Benchmarks for diffuse interface modelling of fluid–solid interactions in a flow

IOP Publishing Modelling Simul. Mater. Sci. Eng. 34 (2026) 015023 https://doi.org/10.1088/1361-651X/ae362c

Modelling and Simulation in Materials Science and Engineering

OPEN ACCESS

RECEIVED
14 October 2025

REVISED
17 December 2025

ACCEPTED FOR PUBLICATION
9 January 2026

PUBLISHED
22 January 2026

PAPER

Benchmarks for diffuse interface modelling of fluid–solid interactions in a flow

Martin Reder[1,2,4,*], **Marcel Weichel**[2,3,4,*], **Britta Nestler**[1,2,3] **and Daniel Schneider**[1,2,3]

[1] Institute of Digital Materials Science, Karlsruhe University of Applied Sciences, Moltkestraße 30, 76133 Karlsruhe, Germany
[2] Institute for Applied Materials—Microstructure Modelling and Simulation, Karlsruhe Institute of Technology (KIT), Straße am Forum 7, 76131 Karlsruhe, Germany
[3] Institute of Nanotechnology (INT), Karlsruhe Institute of Technology (KIT), Hermann-von-Helmholtz-Platz 1, 76344 Eggenstein-Leopoldshafen, Germany
[4] These authors contributed equally to this work.
[*] Authors to whom any correspondence should be addressed.

E-mail: martin_dominik.reder@h-ka.de and marcel.weichel@kit.edu

Keywords: phase-field method, fluid flow, diffuse interface approximation, moving walls

Supplementary material for this article is available online

Abstract

Models based on the coupling of phase-field methods with fluid dynamics are commonly used to simulate flow in complex geometries or in conjunction with phase transformation. Thereby, diffuse interfaces between fluid and solid are used, which requires the corresponding diffusive application of the boundary conditions with regard to the flow. While different approaches to achieving this are found in literature, a quantitative comparison of these methods is still missing. The present work aims to establish benchmarks addressing the diffuse fluid–solid transition for interfaces with and without wall velocity. Furthermore, different models from literature are revisited and comparatively discussed in detail. Using the defined benchmark cases, a quantitative assessment of these models is performed to investigate their accuracy for varying interface widths and different phase-field profiles. The results show that the best choice of the diffuse model is problem-dependent.

1. Introduction

Diffuse interface approaches, such as the phase-field method, can be used for geometry parametrisation of complex domains, which are embedded in a larger domain exhibiting a simple geometry, e.g. a cuboid. This enables large flexibility regarding the numerical discretisation and avoids the necessity of body-fitted meshes [58], as the surface is implicitly tracked by the phase-field variable. Furthermore, the absence of a mesh adaptation due to moving surfaces eliminates the requirement for additional computational power, thus enhancing efficiency and facilitates large-scale simulations [14, 43, 59]. Moreover, phase-field models can be thermodynamically derived from a free energy functional yielding a description of interfacial energies and interface dynamics [20, 24, 57]. Therefore, phase-field methods have been applied in a wide range of materials science and engineering processes, demonstrating their versatility to study fuel cells [27, 36], drying processes of battery electrodes [60], additive manufacturing [19, 41] and martensitic growth [42, 55]. Furthermore, problems including different physically distinguishable domains can be addressed as e.g. for problems in fluid-structure interaction [6, 39, 44, 51], multiphase flow [1, 40, 50] including contact line dynamics [4, 31, 33, 47], or for tracking ferro-electric domains [10, 22]. This includes problems in which certain governing equations are only defined in subdomains. As an example, in context of solidification, the computational domain to account for fluid flow is restricted to liquid regions, while concentration evolution may be defined both in fluid and solid [5]. This finds application in investigating the influence of melt convection during solidification on the morphology of the resulting material [13, 17] highlighting the relevance of such fluid–solid interactions in material science. The use of diffuse interface approaches often requires the application of different

boundary conditions (Dirichlet, Neumann, Robin) across the diffuse transition region between two distinct regions. Li *et al* [37] present a general framework to diffusively apply such boundary condition to a partial differential equation (PDE), which is already used, for example, in the general context of battery intercalation systems [16]. This approach is based on a whole domain formulation derived from the corresponding sharp interface problem as well as on the use of diffuse approximations for indicator functions and the surface Dirac distribution. Thereby, a number of different diffuse approximations is presented in [37], and further higher-order approximations are introduced in [61]. Regarding fluid–solid interfaces, this approach is adapted, e.g. by Aland *et al* [3] and Guo *et al* [25] to formulate a diffuse domain Navier–Stokes model. Another method to treat diffuse fluid–solid interfaces is given by Beckermann *et al* [5] which, in contrast to the aforementioned models, is derived using an ensemble averaging method similarly to models for porous media cf, e.g., [2]. This procedure gives rise to a dissipative fluid–solid interaction term, which is modelled by Beckermann *et al* [5] using a Darcy-type approach and fitted to the Poiseuille flow.

The number of different models and approximations for diffuse fluid–solid interfaces raises the question of their comparative accuracy. Since computational cost limits the affordable resolution for large-scale simulation applications, arbitrarily small diffuse interfaces cannot be employed. Thus, the larger the diffuse interfaces are, the more important the model accuracy becomes for finite interface widths. Benchmark setups with a proper reference solution enable the accuracy of different models to be quantified and help to evaluate errors that arise from diffuse approximations at certain interface widths. By this, benchmarks do not only increase the reliability of results obtained by phase-field simulations, but also provide information as to which model formulation is most beneficial in specific setups. A prominent benchmark case regarding fluid–solid interactions is the flow past a cylinder at different Reynolds numbers, which is used e.g. for benchmarking of immersed boundary methods [35] or mesh free solving methods [12]. The work of Gautier *et al* [23] provides a reference solution for such a flow, which is also employed in this work. Recently, benchmarks for various phase-field models were established e.g. with regards to chemo-mechanics [32], triple junction dynamics [15], or the phase-field crystal method [48]. Furthermore, the bubble rise benchmark of Hysing *et al* [29] was adapted by Aland *et al* [3] to compare different phase-field based two-phase flow models. Contributing to this effort of establishing benchmarks to quantify the accuracy of different phase-field models, the present work aims to provide benchmarks for diffuse fluid–solid interface modelling which are used to compare different model formulations. While phase-field based models for fluid-structure interaction considering a (visco)-elastic solid phase are available [39, 44], the present work addresses problems with rigid solids, where no momentum equations are solved within the solid domain. Thereby, the present work includes studies for both well- and obstacle-type potential profiles. So far, diffuse model formulations for the fluid–solid transition are only used with well-type potential equilibrium profiles. Since the obstacle potential is very commonly used, particularly for modelling solidification processes, see [18], it is also included here. Three benchmark cases are considered, including Poiseuille and Couette channel flows, a flow past a cylinder, using the benchmark from [23], and a boundary layer flow with permeable and impermeable walls. Therefore, a number of different relevant boundary conditions are investigated, including a fixed wall, a movable wall and a permeable wall.

The paper is structured as follows. Firstly, the theory behind the different models is introduced, starting with a derivation from the sharp interface formulation in section 2.1, followed by a detailed discussion of the diffuse interface approximations in section 2.2 and a general overview of the phase-field method in sections 2.3 and 2.4. The results of applying the models in the benchmark examples considered are given in sections 3.1–3.3 for the channel flow, cylinder flow and boundary layer flow.

2. Mathematical formulation

2.1. Sharp interface and whole domain formulation

We consider problems within a computational domain $\Omega = \Omega_\mathrm{f} \cup \Omega_\mathrm{s}$, which comprises the domains $\Omega_\mathrm{f}(t)$ and $\Omega_\mathrm{s}(t)$ taken by fluid and solid, respectively (see figure 1). Thereby, the subdomains may change over time t, while the total domain Ω is considered to be constant over time. Furthermore, the fluid solid interface Γ_fs is given as $\Gamma_\mathrm{fs}(t) = \partial\Omega_\mathrm{f} \cap \partial\Omega_\mathrm{s}$. Assuming an incompressible flow of a Newtonian fluid with homogeneous dynamic viscosity μ, the governing Navier–Stokes system may be written as

$$\rho\dot{\boldsymbol{u}} = -\nabla p + \rho \boldsymbol{f}^\mathrm{b} + \mu\Delta\boldsymbol{u}, \qquad \boldsymbol{x} \in \Omega_\mathrm{f}, \tag{1a}$$

$$\nabla \cdot \boldsymbol{u} = 0, \qquad \boldsymbol{x} \in \Omega_\mathrm{f}. \tag{1b}$$

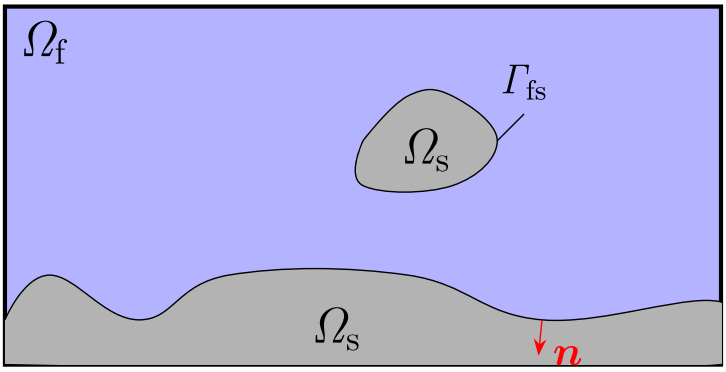

Figure 1. Sketch of the computational domain $\Omega = \Omega_\mathrm{f} \cup \Omega_\mathrm{s}$, the considered subdomains and the corresponding fluid solid interface $\Gamma_\mathrm{fs} = \partial\Omega_\mathrm{f} \cap \partial\Omega_\mathrm{s}$. The outward-pointing normal vector of the fluid domain is denoted as $\boldsymbol{n}$.

Here, ρ denotes the mass density, $\boldsymbol{u}$ the velocity field, p the pressure and $\boldsymbol{f}^\mathrm{b}$ a body force, e.g. gravity. This system of PDEs contains the Navier–Stokes equation (1*a*) which is yielded by inserting the linear viscous constitutive law $\boldsymbol{\sigma} = -p\mathbf{1} + \mu\left(\nabla\boldsymbol{u} + \nabla\boldsymbol{u}^\top\right)$ for the Cauchy stress $\boldsymbol{\sigma}$ into the local momentum balance. Thereby, $\mathbf{1}$ denotes the unit tensor and $(\cdot)^\top$ a transposition. Furthermore, due to incompressibility, the mass balance reduces to the continuity equation (1*b*) as a second PDE in the system (1). It is also noted that due to continuity, $\rho\dot{\boldsymbol{u}} = \partial_t(\rho\boldsymbol{u}) + \nabla\cdot(\rho\boldsymbol{u}\otimes\boldsymbol{u})$ holds. The present work focuses on the treatment of the no-slip boundary condition

$$\forall\ \boldsymbol{x} \in \Gamma_\mathrm{fs}: \quad \boldsymbol{u}(\boldsymbol{x},t) = \boldsymbol{u}^\mathrm{w}(\boldsymbol{x},t)\,, \tag{2}$$

which must be applied to the fluid–solid interface Γ_fs, with $\boldsymbol{u}^\mathrm{w}$ denoting the velocity of the solid wall. Using the indicator function

$$I = \begin{cases} 1 & \boldsymbol{x} \in \Omega_\mathrm{f} \\ 0 & \text{otherwise} \end{cases}, \tag{3}$$

the boundary value problem consisting of (1) and (2) can be transformed to a whole domain formulation, which applies to $\boldsymbol{x} \in \Omega$. Following the ansatz from Li *et al* [37], the whole domain formulation reads

$$I\rho\dot{\boldsymbol{u}} = -I\nabla p + I\rho\boldsymbol{f}^\mathrm{b} + \nabla\cdot(I\mu\nabla\boldsymbol{u}) + (\boldsymbol{u}-\boldsymbol{u}^\mathrm{w})\,\nabla\cdot(\mu\nabla I)\,, \quad \boldsymbol{x}\in\Omega, \tag{4a}$$

$$0 = I\nabla\cdot\boldsymbol{u} + (\boldsymbol{u}-\boldsymbol{u}^\mathrm{w})\cdot\nabla I, \quad \boldsymbol{x}\in\Omega, \tag{4b}$$

and contains both the field equations and boundary conditions. The corresponding derivation is shown in appendix. Note that the gradient ∇I of the indicator function is given by the outward-pointing normal $\boldsymbol{n}$ of the fluid domain and the surface Dirac distribution δ^fs via

$$\nabla I(\boldsymbol{x},t) = -\delta^\mathrm{fs}(\boldsymbol{x},t)\ \boldsymbol{n}(\boldsymbol{x},t)\,. \tag{5}$$

Some of the terms in equation system (4) can be reformulated. Exploiting $I\nabla\cdot\boldsymbol{u} = \nabla\cdot(I\boldsymbol{u}) - \boldsymbol{u}\cdot\nabla I$, the whole domain continuity equation becomes

$$0 = \nabla\cdot(I\boldsymbol{u}) + \delta^\mathrm{fs}\boldsymbol{u}^\mathrm{w}\cdot\boldsymbol{n}. \tag{6}$$

An alternative formulation of the right-hand side of equation (4*a*) is given by

$$I\rho\dot{\boldsymbol{u}} = -I\nabla p + I\rho\boldsymbol{f}^\mathrm{b} + \nabla\cdot[\mu\nabla(I\boldsymbol{u})] - \mu(\nabla\boldsymbol{u})\nabla I - \boldsymbol{u}^\mathrm{w}\nabla\cdot(\mu\nabla I)\,, \tag{7}$$

as shown in appendix A.2.2. Additionally, the term $I\rho\dot{\boldsymbol{u}}$ can be reformulated to

$$\frac{\partial(I\rho\boldsymbol{u})}{\partial t} + \nabla\cdot(I\rho\boldsymbol{u}\otimes\boldsymbol{u})\,, \tag{8}$$

in absence of phase-transformation or molecular diffusion between solid and fluid, and thus, $\dot{I} = \partial_t I + \boldsymbol{u}\cdot\nabla I = 0$, cf appendix A.2.1. This is the case, if either the dividing surface between the fluid and solid domains is transported with the boundary velocity $\boldsymbol{u}^\mathrm{w}$, if the wall velocity is purely tangential $\boldsymbol{u}^\mathrm{w}\cdot\boldsymbol{n} = 0$, or if the interface does not move with the wall velocity, e.g. by applying boundary conditions which mimic uniform blowing or suction.

2.2. Diffuse interface model

Based on the whole domain formulation introduced in section 2.1, a diffuse interface model is derived. To this end, the phase-field tuple $\boldsymbol{\phi} = \{\phi_1, \ldots, \phi_N\}$ is introduced for a number of N phases, where for each phase α, the phase variable $\phi_\alpha(\boldsymbol{x}, t)$ is defined. Similar to the indicator function, a phase variable defines whether the point $\boldsymbol{x}$ is associated to phase α, at a certain time t. However, instead of sharply jumping from 0 to 1, at the interface between two phases, the phase variable exhibits a smooth transition over a finite region of width δ_d, which is called the diffuse interface. Within this diffuse interface, a mixture of phases occurs, and ϕ_α can be seen as local volume fraction of phase α. The phase variables are subjected to the summation constraint

$$\forall\, \boldsymbol{x} \in \Omega,\ t \geqslant 0: \quad \sum_{\alpha=1}^{N} \phi_\alpha(\boldsymbol{x}, t) = 1. \tag{9}$$

Furthermore, the bulk region of phase α is defined as

$$\Omega_{\phi_\alpha=1}(t) = \{\boldsymbol{x} \in \Omega: \quad \phi_\alpha(\boldsymbol{x}, t) = 1\}, \tag{10}$$

and its region of occurrence as

$$\Omega_{\phi_\alpha>0}(t) = \{\boldsymbol{x} \in \Omega: \quad \phi_\alpha(\boldsymbol{x}, t) > 0\}. \tag{11}$$

Furthermore, the diffuse interface between the phases α and $\beta \neq \alpha$ is

$$\Gamma^\mathrm{d}_{\alpha\beta}(t) = \Omega_{\phi_\alpha>0} \cap \Omega_{\phi_\beta>0}. \tag{12}$$

Note that problems consisting of multiple fluid and solid phases can be considered as pseudo-two-phase problems of the total fluid phase ϕ^f and solid phase ϕ^s, which are the sum of all individual fluid and solid phases, respectively (cf, e.g., [49]). In such a case, the interpolation of viscosity and density for the fluid must exclude the solid phases. Thus, e.g. a linear interpolation scheme for the mixture fluid density of N_fluid fluid phases takes the form

$$\rho_\mathrm{fluid} = \frac{1}{\phi^\mathrm{f}} \sum_{\alpha=1}^{N_\mathrm{fluid}} \phi_\alpha \rho_\alpha, \qquad \phi^\mathrm{f} = \sum_{\alpha=1}^{N_\mathrm{fluid}} \phi_\alpha. \tag{13}$$

This allows to consider multiphase problems by using a two-phase diffuse Navier–Stokes system in terms of ϕ^f and $\phi^\mathrm{s} = 1 - \phi^\mathrm{f}$ without any restrictions. Therefore, for the sake of simplicity, the model equations in this paper are written in the form of a two-phase problem, i.e. $N = 2$. Due to the summation constraint (9), only one phase variable is independent, and therefore, the abbreviation $\phi := \phi_1$ is used for the phase-field variable related to the fluid, while $\phi_2 = 1 - \phi$ is associated with the solid.

Diffuse approximations of the whole domain equations. The straightforward way of retrieving a diffuse interface formulation for the Navier–Stokes system is to use the whole domain formulation (4) and replace the indicator function I and its gradient, and thus, the surface Dirac distribution, by suitable diffuse approximations, depending on the phase field ϕ [62]. To this end, the approximations

$$I \approx h(\phi) \quad \text{and} \quad \delta_\Gamma \approx \frac{\partial h}{\partial \phi} \|\nabla \phi\| \tag{14}$$

can be used with a so-called interpolation function h [45]. However, the simplest choice is using $h = \phi$ directly, as previously employed in other studies [37, 62]. In this work, such direct approximations for equation (4*a*) or (7) are labelled as Li-type direct approximation (LDA) and Beckermann-type direct approximation (BDA), respectively. The interpolation function h requires to meet the conditions $h(0) = 0$, $h(1) = 1$ and $\int_0^1 h(\phi)\, \mathrm{d}\phi = 1$. A variety of options for this interpolation function are available and discussed, for example, in [26]. Higher-order polynomials like $h = \phi^2(3 - 2\phi)$ steepen the transition of h, compared to ϕ, in the vicinity of $\phi = 1/2$ and flatten it on the outskirts of the diffuse interface. Irrespective of the choice made for h, the diffuse approximation converges to the sharp interface equation (4) in the limit of $\delta_\mathrm{d} \to 0$. In this work, only $h = \phi$ is considered, since a steeper transition can also be achieved by applying smaller interface widths δ_d. Furthermore, restrictions regarding steepness usually arise from the requirement to sufficiently resolve the transition with numerical discretisation [18]. Various other diffuse approximations of the viscous term $\boldsymbol{M} := \nabla \cdot (I\mu\nabla\boldsymbol{u}) + (\boldsymbol{u} - \boldsymbol{u}^\mathrm{w})\nabla \cdot$

$(\mu\nabla I)$ in the sharp interface problem with Dirichlet boundary conditions are given by Li *et al* [37, equations (2.21)–(2.24)]. Their approximation 4 corresponds to LDA, and thus, directly uses $I \approx \phi$, while their approximations 1 to 3 differ and are justified by showing that they converge in the sharp interface limit $\delta_\mathrm{d} \to 0$. Subsequently, they are briefly revised and discussed.

First Li-type approximation. The approximation 1 of Li *et al* [37], subsequently abbreviated as LA1, yields the viscous term

$$\boldsymbol{M} \approx \nabla \cdot (\phi\mu\nabla\boldsymbol{u}) + \mu\,(\boldsymbol{u}-\boldsymbol{u}^\mathrm{w})\,\tilde{\beta}\frac{(\phi-1)}{\varepsilon^3}, \tag{15}$$

where the interface width parameter $\varepsilon \propto \delta_\mathrm{d}$ and $\tilde{\beta}$ is a proportionality factor. The original approximation from [37] is introduced for $\tilde{\beta}=1$, and thus, omitting the proportionality factor of the distribution function $(\phi-1)/\varepsilon^3$. The generalisation of this approximation is introduced by Aland *et al* [3], where they show that it converges to in the sharp interface limit for any choices of $\tilde{\beta} \propto 1$ or $\tilde{\beta} \propto \varepsilon$. While Aland *et al* [3] still use the original distribution function $(\phi-1)/\varepsilon^3$ with $\tilde{\beta}=1$, Guo *et al* [25] employ $\tilde{\beta}=\varepsilon$, and therefore, the distribution function $(\phi-1)/\varepsilon^2$. In the present work, we stick to the original formulation $\tilde{\beta} \propto 1$, since the other option $\tilde{\beta} \propto \varepsilon$ leads to significantly larger error results, compared to the original choice $\tilde{\beta}=1$ in the basic benchmark cases of Couette and Poiseuille flow. Writing equation (15) in terms of the interface thickness definition from the present work yields

$$\boldsymbol{M} \approx \nabla \cdot (\phi\mu\nabla\boldsymbol{u}) + \mu\,(\boldsymbol{u}-\boldsymbol{u}^\mathrm{w})\,\beta\frac{(\phi-1)}{\delta_\mathrm{d}^3}. \tag{16}$$

The work of Li *et al* [37] employs a tanh-profile (see equation (24)) for the phase field ϕ, and their definition of the interface length parameter ε corresponds to $\varepsilon = \delta_\mathrm{d}/2$. Therefore, $\beta = 8\tilde{\beta} = 8$ recovers the approximation 1, as used in [3, 37]. For the sin-type phase-field profile additionally investigated in this work, a pre-factor $\beta = 5.0685$ is used.

Second Li-type approximation. Furthermore, the approximation 2 from [37] is considered within this work under the abbreviation LA2, for which the viscous term is approximated as

$$\boldsymbol{M} \approx \nabla \cdot (\mu\nabla\boldsymbol{u}) - \mu\,(\boldsymbol{u}-\boldsymbol{u}^\mathrm{w})\,\frac{B(\phi)}{\varepsilon^3} \tag{17}$$

with $B(\phi) \propto \phi^2(1-\phi)^2$ used as a distribution function. As shown in [37], the sharp interface limit is reached for any constant proportionality factor. In this work, $B(\phi) = 30\tilde{\beta}\phi^2(1-\phi)^2$ is chosen in order to meet $\int_0^1 30\phi^2(1-\phi)^2\,\mathrm{d}\phi = 1$. Formulating it in terms of the present interface thickness definition δ_d, This approximation yields

$$\boldsymbol{M} \approx \nabla \cdot (\mu\nabla\boldsymbol{u}) - \mu\,(\boldsymbol{u}-\boldsymbol{u}^\mathrm{w})\,\frac{30\beta\phi^2\,(1-\phi)^2}{\delta_\mathrm{d}^3}. \tag{18}$$

Beckermann-type approximation. Besides the approximations in [37], the diffuse model by Beckermann *et al* [5] is a widely used diffuse interface approximation. It is originally derived based on the volume averaging approach. However, as shown in this work, it can also be derived from the whole domain formulation using equation (7) and the approximation $I \approx \phi$. As presented in section 2.1, this formulation is analytically identical to equation (4*a*). Furthermore, Beckermann *et al* [5] introduce a model expression for the term $\mu(\nabla\boldsymbol{u})\nabla I$, instead of directly evaluating it, which yields the approximation

$$\mu(\nabla\boldsymbol{u})\nabla\phi \approx h_\mathrm{f}\mu\,(\boldsymbol{u}-\boldsymbol{u}^\mathrm{w})\,\frac{1-\phi}{\delta_\mathrm{d}}\|\nabla\phi\|, \tag{19}$$

with the dimensionless friction coefficient h_f. Subsequently, this is referred to as Beckermann friction approximation (BFA). For more details, especially regarding the choice of h_f, we refer to appendix A.2. This approach yields the viscous term

$$\boldsymbol{M} \approx \nabla \cdot [\mu\nabla(\phi\boldsymbol{u})] - h_\mathrm{f}\mu\,(\boldsymbol{u}-\boldsymbol{u}^\mathrm{w})\,\frac{1-\phi}{\delta_\mathrm{d}}\|\nabla\phi\| - \boldsymbol{u}^\mathrm{w}\nabla\cdot(\mu\nabla\phi). \tag{20}$$

It should be noted that Beckermann *et al* [5] derived their model for a wall velocity of zero $\boldsymbol{u}^\mathrm{w} = \boldsymbol{0}$ and that the slight extension to the more general case is introduced here for the first time.

Table 1. Overview of the different diffuse interface models for the viscous term $\boldsymbol{M}$. For a well-type tanh-profile, $\beta = 8$ and $h_\mathrm{f} = 33.126$ are employed, while for an obstacle-type sin-profile, $\beta = 5.0685$ and $h_\mathrm{f} = 19.721$ are chosen. Details on the fitted values of h_f cf can be found in appendix A.2.

Abbreviation	Approximation of $\boldsymbol{M}$ (viscous and boundary term)
LDA	$\nabla\cdot(\phi\mu\nabla\boldsymbol{u}) + (\boldsymbol{u}-\boldsymbol{u}^\mathrm{w})\nabla\cdot(\mu\nabla\phi)$
LA1	$\nabla\cdot(\phi\mu\nabla\boldsymbol{u}) - \mu(\boldsymbol{u}-\boldsymbol{u}^\mathrm{w})\frac{\beta(1-\phi)}{\delta_\mathrm{d}^3}$
LA2	$\nabla\cdot(\mu\nabla\boldsymbol{u}) - \mu(\boldsymbol{u}-\boldsymbol{u}^\mathrm{w})\frac{30\beta\phi^2(1-\phi)^2}{\delta_\mathrm{d}^3}$
BDA	$\nabla\cdot[\mu\nabla(\phi\boldsymbol{u})] - \mu(\nabla\boldsymbol{u})\nabla\phi - \boldsymbol{u}^\mathrm{w}\nabla\cdot(\mu\nabla\phi)$
BFA	$\nabla\cdot[\mu\nabla(\phi\boldsymbol{u})] - h_\mathrm{f}\mu(\boldsymbol{u}-\boldsymbol{u}^\mathrm{w})\frac{1-\phi}{\delta_\mathrm{d}}\|\nabla\phi\| - \boldsymbol{u}^\mathrm{w}\nabla\cdot(\mu\nabla\phi)$

Overview of the compared models. This section provides an overview of all the different diffuse model formulations of the whole domain Navier–Stokes equation (4*a*) from the previous section. It can be written as

$$I\rho\dot{\boldsymbol{u}} = -I\nabla p + I\rho\boldsymbol{f}^\mathrm{b} + \boldsymbol{M}, \tag{21}$$

with

$$\begin{aligned}\boldsymbol{M} &= \nabla\cdot(I\mu\nabla\boldsymbol{u}) + (\boldsymbol{u}-\boldsymbol{u}^\mathrm{w})\,\nabla\cdot(\mu\nabla I)\\ &= \nabla\cdot[\mu\nabla(I\boldsymbol{u})] - \mu(\nabla\boldsymbol{u})\nabla I - \boldsymbol{u}^\mathrm{w}\nabla\cdot(\mu\nabla I)\,,\end{aligned} \tag{22}$$

comprising the bulk and the boundary part of the viscous term from the whole domain Navier–Stokes equation (4*a*). All diffuse models share the terms $I\rho\dot{\boldsymbol{u}}$, $-I\nabla p$ and $I\rho\boldsymbol{f}^\mathrm{b}$ and approximate them by using $I \approx \phi$. For $\boldsymbol{M}$, the different approximations are summarised in table 1.

2.3. Phase-field profiles and interface width definition

In case of the phase-field method (PFM), which is only used for geometry parametrisation of a known sharp interface Γ, the values of ϕ can directly be prescribed with the coordinate η in interface normal direction, which is a signed distance function with respect to Γ, and defined as

$$\eta(\boldsymbol{x},t) = \min_{\boldsymbol{x}'\in\Gamma(t)} \|\boldsymbol{x}-\boldsymbol{x}'\|. \tag{23}$$

Any function $\phi(\eta)$ varying monotonically between 1 to 0 for $-\delta_\mathrm{d}/2 \leqslant \eta \leqslant \delta_\mathrm{d}/2$ can be chosen to prescribe the phase-field profile. Alternatively, a PDE that describes the phase-field evolution must be considered giving rise to the phase-field variable ϕ, as discussed in section 2.4. For prescribing the course of phase-field variables within the diffuse interface, different options are available. Two very common phase-field profiles are given as

$$\phi^\mathrm{t}(\eta) = \frac{1}{2}\left[1-\tanh\left(\frac{6\eta}{\delta_\mathrm{d}}\right)\right] \quad \text{and} \quad \phi^\mathrm{s}(\eta) = \frac{1}{2}\left[1-\sin\left(\frac{\pi\eta}{\delta_\mathrm{d}}\right)\right] \tag{24}$$

inside the diffuse interface Γ^d (see equation (12)), which is characterised by $-\delta_\mathrm{d}/2 \leqslant \eta \leqslant \delta_\mathrm{d}/2$. The corresponding normal gradients $\nabla\phi\cdot\boldsymbol{n} = \partial_\eta\phi = -\|\nabla\phi\|$ can be expressed as

$$\nabla\phi^\mathrm{t}\cdot\boldsymbol{n} = -\frac{12}{\delta_\mathrm{d}}\phi^\mathrm{t}\left(1-\phi^\mathrm{t}\right) \quad \text{and} \quad \nabla\phi^\mathrm{s}\cdot\boldsymbol{n} = -\frac{\pi}{\delta_\mathrm{d}}\sqrt{\phi^\mathrm{s}(1-\phi^\mathrm{s})}. \tag{25}$$

Both the profiles and the normal gradients are visualised in figure 2.

If the signed distance $\eta(\boldsymbol{x},t)$ to the interface is known, the phase-field profile is set by the piecewise definition

$$\phi(\boldsymbol{x},t) = \begin{cases} 1 & \eta(\boldsymbol{x},t) \leqslant -\delta_\mathrm{d}/2 \\ 0 & \eta(\boldsymbol{x},t) \geqslant \delta_\mathrm{d}/2 \\ \phi^{\mathrm{t/s}}(\eta) & \text{otherwise} \end{cases}. \tag{26}$$

It is noted, that for the tanh-type profile, a cut-off definition is used, since ϕ^t only asymptotically approaches 1 and 0 for $\eta \to \mp\infty$, respectively. In the present work, the cut-off is considered at $\tanh(\pm 3)$, and thus at the values $\phi^- := \phi^\mathrm{t}(-\delta_\mathrm{d}/2) \approx 0.9975$ and $\phi^+ := \phi^\mathrm{t}(+\delta_\mathrm{d}/2) \approx 0.0025$. Instead of continuing the tanh-profile for $|\eta| \geqslant \delta_\mathrm{d}/2$, the ϕ-values are directly set to the bulk values 1 and 0 in

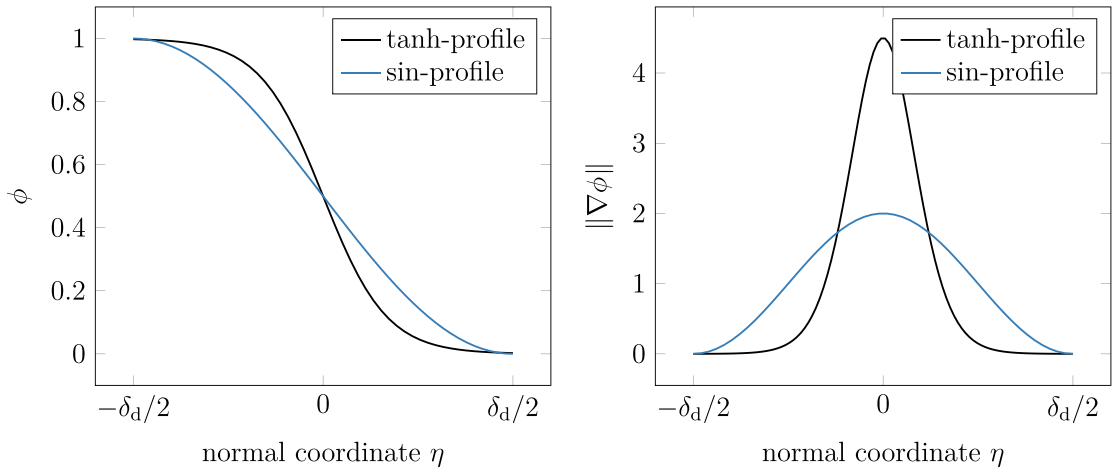

Figure 2. Equilibrium phase-field profiles for well and obstacle potential, according to equation (24), and the corresponding normal gradients, according to equation (25), plotted over the interface normal coordinate η.

the numerical implementation giving rise to a small jump of ± 0.0025. Different cut-off definitions are employed in literature, e.g. $\tanh(\pm 3/2)$ is used in [5], yielding a cut-off at $\phi^- \approx 0.953$ and $\phi^+ \approx 0.047$, respectively. For the sin-type profile, no such cut-off is required, since a finite interface width of δ_d is naturally obtained.

2.4. Phase-field potential and equations

Instead of directly prescribing phase-field variables by the signed distance function η to a known interface for a geometry parametrisation, the PFM is often used for implicit tracking of evolving interfaces, e.g. to model phase evolution and transformation processes. In such a case, the phase-field variables are determined from a system of PDEs, which are typically derived by a variational principle based on maximisation of an entropy or minimisation of a free energy functional [57]. In this way, the PFM is able to model capillary-driven interface motion [31, 40] or phase transformation processes like solidification [45]. Furthermore, elastics boundary effects can be incorporated, as demonstrated in applications, such as blood vessels [9, 63]. Subsequently, this is briefly introduced for the two-phase case, to show the connection of PFM and the diffuse whole domain Navier–Stokes formulation. Consider the free energy functional

$$\mathcal{F}(\phi, \nabla\phi) = \int_\Omega f^{\,\mathrm{grad}}(\phi, \nabla\phi) + f^{\,\mathrm{pot}}(\phi) + f^{\,\mathrm{bulk}}(\phi)\ \mathrm{d}V + \int_{\partial\Omega} f^{\,\mathrm{surf}}(\phi)\ \mathrm{d}S \tag{27}$$

with the corresponding variation

$$\delta\mathcal{F} = \int_\Omega \left(\frac{\partial \left(f^{\,\mathrm{grad}} + f^{\,\mathrm{pot}} + f^{\,\mathrm{bulk}} \right)}{\partial\phi} - \nabla \cdot \frac{\partial f^{\,\mathrm{grad}}}{\partial \nabla\phi} \right) \delta\phi\ \mathrm{d}V + \int_{\partial\Omega} \left(\frac{\partial f^{\,\mathrm{surf}}}{\partial\phi} + \frac{\partial f^{\,\mathrm{grad}}}{\partial \nabla\phi} \cdot \boldsymbol{n} \right) \delta\phi\ \mathrm{d}S. \tag{28}$$

For equilibrium, the free energy is minimised, and thus, the condition $\forall\ \delta\phi\colon\ \delta\mathcal{F} = 0$ is required. The energy density contributions $f^{\,\mathrm{grad}} + f^{\,\mathrm{pot}}$ model interfacial energies and vanish for $\boldsymbol{x} \notin \Gamma^d$, while $f^{\,\mathrm{bulk}}$ denotes a bulk energy density. The surface energy density $f^{\,\mathrm{surf}}$ of the domain boundary $\partial\Omega$ can be used to model surface wetting cf, e.g., [31]. Neglecting bulk energies, i.e. $f^{\,\mathrm{bulk}} = 0$, and modelling the gradient contribution as $f^{\,\mathrm{grad}} = \gamma\epsilon\|\nabla\phi\|^2$ yields the field equation

$$\frac{\partial f^{\,\mathrm{pot}}}{\partial\phi} - 2\gamma\epsilon\Delta\phi = 0 \tag{29}$$

at equilibrium. Here, γ is the surface tension between the two phases, $\epsilon \propto \delta_d$ is a parameter related to the interface thickness and the potential term is often chosen as either the well potential $f^{\,\mathrm{pot}} = 9\gamma/\epsilon\,\phi^2(1-\phi)^2$ or the obstacle potential $\forall\ \boldsymbol{x} \in \Gamma^d\colon\ f^{\,\mathrm{pot}} = 16\gamma/(\pi^2\epsilon)\,\phi(1-\phi)$. For planar interfaces, the tanh- and sin-type profiles from equation (24) are the solutions of the equation with the well and obstacle potential contributions, respectively. Therefore, they are the equilibrium profiles of the respective potential. The relations for the interface width are $\delta_d = 4\epsilon$ and $\delta_d = \pi^2/4\,\epsilon$ for the well and obstacle potential. For curved interfaces, these profiles correspond to the zero order term of a Taylor series

expansion of ϕ in ϵ, where the higher order terms are depending on the curvature [26][equation (70)]. In addition, a solution of equation (29) for curved interfaces will cause one of the phases to vanish. However, if it is augmented with an additional constraint enforcing a certain volume of each phase [8, 34, 46, 53], or if the Cahn-Hilliard-type equation

$$\Delta\left(\frac{\partial f^{\text{pot}}}{\partial\phi} - 2\gamma\epsilon\Delta\phi\right) = 0 \tag{30}$$

is used, non-trivial solutions are possible, giving rise to the profiles (24) as lowest-order term in the Taylor series expansion of ϕ in the interface. This is also the case, if the curvature minimising dynamics of equation (29) is removed by the additional curvature correction term $\|\nabla\phi\|\nabla\cdot\boldsymbol{n}$ with $\boldsymbol{n} = -\nabla\phi/\|\nabla\phi\|$ [58]. This yields the equation

$$0 = \frac{\partial f^{\text{pot}}}{\partial\phi} - 2\gamma\epsilon\left(\Delta\phi + \|\nabla\phi\|\nabla\cdot\boldsymbol{n}\right) = \frac{\partial f^{\text{pot}}}{\partial\phi} - 2\gamma\epsilon\nabla\left(\nabla\phi\cdot\boldsymbol{n}\right)\cdot\boldsymbol{n}, \tag{31}$$

with the Laplace term being substituted by the derivative in interface normal direction [55]. This equation preserves the initial shape of the phase domains and only enforces the equilibrium phase-field profiles [58]. Using this approach, the phase-field method is a tool for implicit geometry parametrisation and does not yield any interface dynamics.

To consider phase changes, phase-field evolution equations are considered, instead of the steady-state equations presented above. As an example, the dynamic version of equation (29) with an Allen-Cahn approach reads

$$\frac{\partial\phi}{\partial t} = M^{\text{AC}}\left(\frac{\partial f^{\text{pot}}}{\partial\phi} - 2\gamma\epsilon\Delta\phi\right), \tag{32}$$

with a mobility parameter M^{AC}. Furthermore, multiphase-field approaches like [45, 56] can be employed. In this case, a quasi two-phase problem for the diffuse Navier–Stokes equation can be retrieved in terms of ϕ^{f} and ϕ^{s}, by summing up all fluid phases to $\phi^{\text{f}}(\boldsymbol{x},t) = \sum\phi^{\text{f}}_{\alpha}(\boldsymbol{x},t)$ and all solid phases to $\phi^{\text{s}}(\boldsymbol{x},t) = \sum\phi^{\text{s}}_{\alpha}(\boldsymbol{x},t)$, respectively [49].

3. Numerical examples comparing interface approximations

The subsequent chapter conducts an investigation into the influence of the interface approximations from table 1 for a range of different benchmarks. These benchmarks involve the Couette and Poiseuille flow, the flow past a cylinder and the boundary layer problem with and without suction.

3.1. Couette and Poiseuille flow

Analytic solution and benchmark quantities

For a stationary flow, which is unidirectional, fully developed, without body force in flow direction, and a fluid with constant viscosity, the Navier–Stokes system reduces to the ordinary differential equation (ODE)

$$0 = \mu\frac{\mathrm{d}^2u}{\mathrm{d}y^2} - \frac{\partial p}{\partial x}, \tag{33}$$

with respect to the velocity component $u := \boldsymbol{u}\cdot\boldsymbol{e}_x$, while the pressure gradient is a constant. For the boundary conditions $u(y=0) = 0$ and $u(y=H) = 0$, this yields a Poiseuille flow, whereas $\partial_x p = 0$, and the upper boundary condition $u(y=H) = u_{\text{top}}$ yields a Couette flow. For the Poiseuille flow, the dimensionless quantities $\tilde{y} := y/H$ and $\tilde{u} := u/u_{\text{c}}$, using the characteristic velocity $u_{\text{c}} = -\partial_x pH^2/(12\mu)$ as the mean velocity, are introduced. The boundary value problem for the Poiseuille flow then becomes

$$0 = \frac{\mathrm{d}^2\tilde{u}}{\mathrm{d}\tilde{y}^2} - 12, \quad \tilde{u}(\tilde{y}=0) = 0, \quad \tilde{u}(\tilde{y}=1) = 0. \tag{34}$$

In the case of the Couette flow, the upper velocity is set to $u_{\text{top}} = u_{\text{c}}$, which results in the boundary value problem

$$0 = \frac{\mathrm{d}^2\tilde{u}}{\mathrm{d}\tilde{y}^2}, \quad \tilde{u}(\tilde{y}=0) = 0, \quad \tilde{u}(\tilde{y}=1) = 1. \tag{35}$$

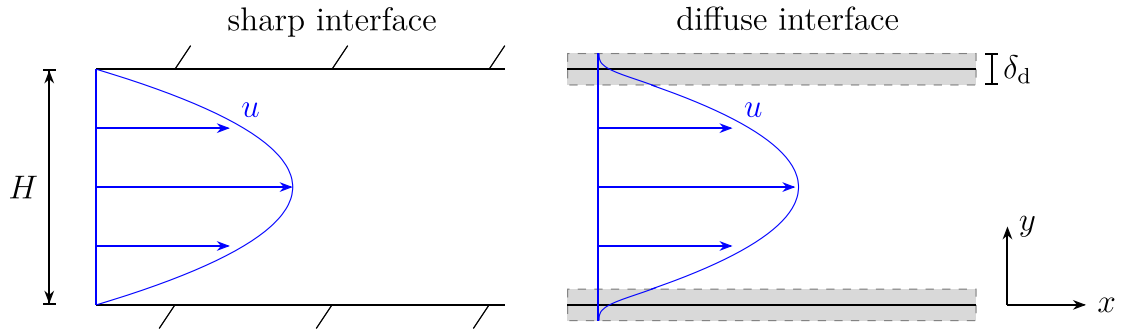

Figure 3. Sketch of the channel considered with sharp and diffuse interface and velocity profiles for Poiseuille flow. In case of Couette flow, the upper wall moves in x-direction, which leads to a linear velocity profile.

For both flows, analytical solutions are available which can be used as benchmark. They read

$$\tilde{u} = -6\tilde{y}(\tilde{y}-1) \quad \text{and} \quad \tilde{u} = \tilde{y} \tag{36}$$

for the boundary value problems (34) and (35), respectively. The whole domain formulation, on the basis of which the diffuse models are used, is defined as

$$0 = \frac{\mathrm{d}}{\mathrm{d}\tilde{y}}\left(I\frac{\mathrm{d}\tilde{u}}{\mathrm{d}\tilde{y}}\right) + (\tilde{u}-\tilde{u}_\mathrm{w})\frac{\mathrm{d}^2 I}{\mathrm{d}\tilde{y}^2} + Ic \tag{37a}$$

$$= \frac{\mathrm{d}^2 I\tilde{u}}{\mathrm{d}\tilde{y}^2} - \frac{\mathrm{d}\tilde{u}}{\mathrm{d}\tilde{y}}\frac{\mathrm{d}I}{\mathrm{d}\tilde{y}} - \tilde{u}_\mathrm{w}\frac{\mathrm{d}^2 I}{\mathrm{d}\tilde{y}^2} + Ic, \tag{37b}$$

with $c = 12$ and $\tilde{u}_\mathrm{w} = 0$ for Poiseuille flow, and $c = 0$ and $\tilde{u}_\mathrm{w} = 1$, at the top, for Couette flow, respectively.

Two benchmark quantities are considered. Firstly, the mean velocity

$$\overline{u} = \frac{1}{H}\int_0^H u\,\mathrm{d}y = \frac{1}{H}\int_{-\infty}^{\infty} Iu\,\mathrm{d}y. \tag{38}$$

Secondly, the relative L_2-error of the velocity field in the bulk region $\Omega_{\phi=1} = [+\delta_\mathrm{d}/2, H-\delta_\mathrm{d}/2]$, defined as

$$e_2 := \int_{\Omega_{\phi=1}} (u-u_\mathrm{ref})^2\,\mathrm{d}y \left(\int_{\Omega_{\phi=1}} (u_\mathrm{ref})^2\,\mathrm{d}y\right)^{-1}, \tag{39}$$

where u_ref denotes the respective analytical solution. The e_2-error measures the accuracy of the local velocity field in the bulk region, and the influence the diffuse boundary has on it. In addition, the error $e_\mathrm{bulk} = (\overline{u}-\overline{u}_\mathrm{ref})/\overline{u}_\mathrm{ref}$ regarding the channel mean velocity is investigated since it also covers the solution inside the diffuse interface and gives rise to the deviation in the global volume flow rate. The setup of the benchmark problem is shown in figure 3.

Simulation setup for model error

The diffuse approximation of the ODE (37) of the whole domain formulation, using $I \approx \phi$, is solved numerically for different diffuse models defined in section 2.2. A finite difference method is employed, and the corresponding code implemented in matlab/GNU octave is provided as supplementary material. Numerical errors are kept negligibly small by using a very fine grid with 12 000 nodes over $[0,H]$ and the total number of nodes as $12000(1+\delta_\mathrm{d}/H)$ for the extended domain $\Omega = [-\delta_\mathrm{d}/2, H+\delta_\mathrm{d}/2]$, considered for the simulations, unless otherwise stated. The linear equation system is solved directly to avoid iteration errors. All simulations were executed with the equilibrium profile of both the obstacle and the well potential.

Discussion of the Poiseuille flow results

Figure 4 shows the two benchmark quantities as a function of the interface thickness, in relation to the height of the channel H, for two distinct potential terms. The left-hand column shows the relative error $e_\mathrm{bulk} = (\overline{u}-\overline{u}_\mathrm{ref})/\overline{u}_\mathrm{ref}$, while the right column illustrates the L_2-error, according to equation (39). Each

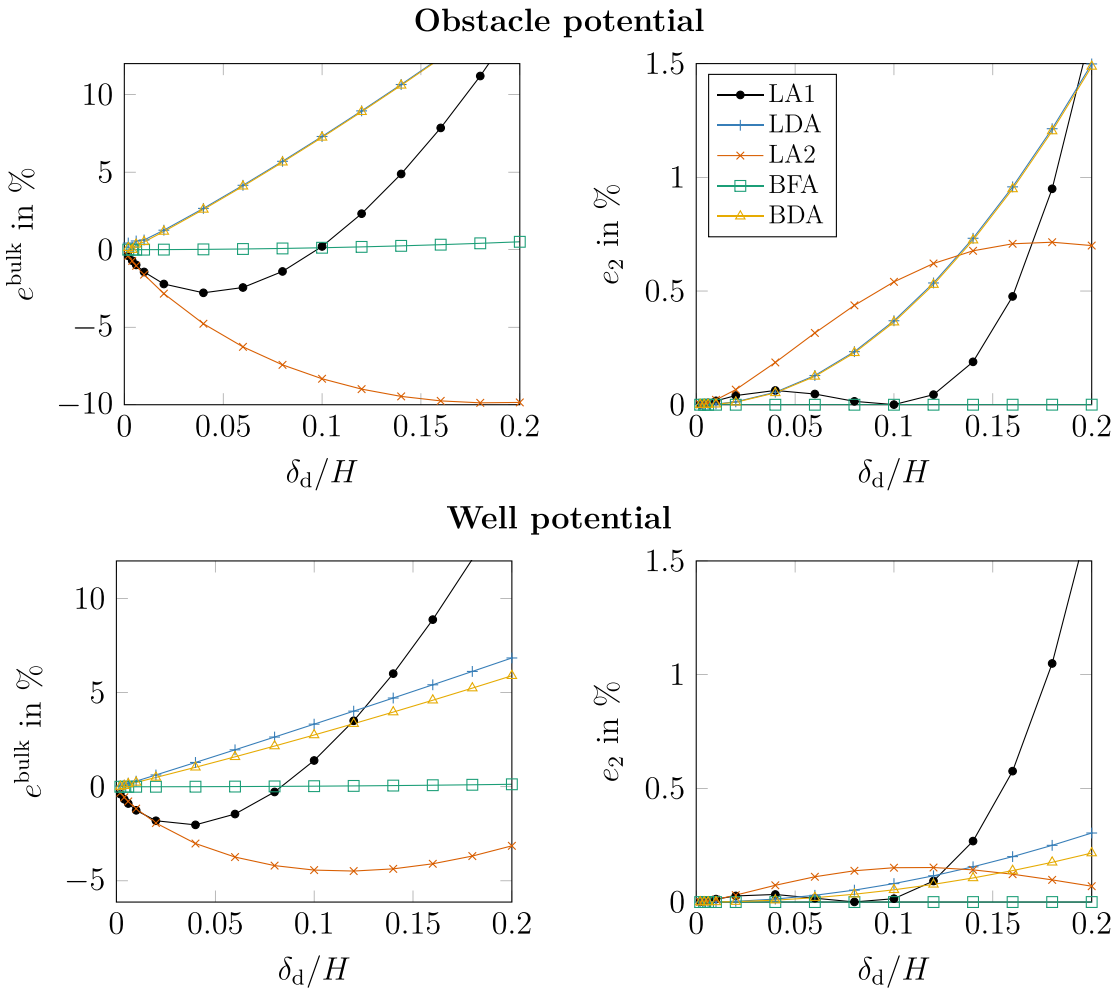

Figure 4. Model errors of the different diffuse approximations for Poiseuille flow at various interface thicknesses. Left: Relative error $e_{\text{bulk}} = (\overline{u} - \overline{u}_{\text{ref}})/\overline{u}_{\text{ref}}$ regarding the bulk velocity $\overline{u}$ (cf equation (38)). Right: L_2-error regarding the velocity field according to equation (39).

model is distinguished by specific colour coding, with black, blue, orange, green and yellow assigned to the models LA1, LDA, LA2, BFA and BDA, respectively.

Obstacle potential. The first row of figure 4 depicts the relative error measures for an obstacle potential. In the case of the model BFA, the smallest possible relative and L_2-errors are demonstrated. These are generally errors close to zero that show a monotone decrease for decreasing interface thickness, with errors of $e_{\text{bulk}} = 0.5\%$ and $e_2 = 0.0003\%$ at the largest interface width. The reason for these minor errors is that the approximation parameter h_f used has been fitted using Poiseuille flow [5], and thus, the expected behaviour is a very good agreement for this benchmark case. As seen in figure 4, the two direct model variants, namely LDA and BDA, yield approximately identical errors which differ by less than 0.1% for all thicknesses. While overestimating the bulk velocity, the error e_{bulk} decreases approximately linearly with decreasing interface width, and the L_2-error decreases with quadratic shape. For the error e_{bulk}, approximation LA1 shows non-monotone convergence with an error close to zero at a thickness $\delta_d = 0.1H$. Subsequently, a local maximum error at $\delta_d \approx 0.05H$ is observed, before the error decreases again towards the sharp interface limit. This behaviour is accompanied by a sign change for e_{bulk}, where the bulk velocity is underestimated for $\delta_d < 0.1H$ and overestimated for $\delta_d > 0.1H$. For relatively large interface widths, the LA1 introduces larger errors compared to LDA. All three approximation models yield relatively poor behaviour at large interface widths, leading to deviations of above 10% and 1% for the relative error and the L_2-error, respectively. Finally, the LA2 model shows a poor behaviour for small interface widths, which is even worse than LDA, for a thickness below $0.125H$, before the errors decrease to the sharp interface limit. However, at large interface widths, LA2 performs better than LDA. In particular, the error seems to be bounded and asymptotically reaches values of $e_{\text{bulk}} = -10\%$ and $e_2 = 0.75$ %. However, such large interfaces are of limited practical relevance, since

diffuse interface widths are typically considered to be significantly smaller, compared to the physical length scale. For smaller interface widths below 10% of the channel height, the approximations BFA and LA1 achieve the best results.

Well potential. The results for the well potential, plotted in the second row of figure 4, largely exhibit behaviour similar in quality to that of the obstacle potential. In contrast to the obstacle potential, the LDA and BDA models demonstrate minor deviations. These deviations increases with the interface thickness and reaches approximately 1% for the largest interface considered. Even though these models are analytically identical, a significant difference is introduced in this case, due to the cut-off which becomes necessary for the tanh-profile. Both direct models generally have fewer errors, compared to the obstacle potential. A similar observation can be made for LA2. Regarding the LA1 model, the errors are in a very similar range, compared to the obstacle case. However, the extremum of the errors are shifted a bit more towards smaller δ_d.

Conclusion. In summary, all diffuse approximations converge to the analytical solution in the limiting case $\delta_\mathrm{d} \to 0$. However, the quality of the approximations differs significantly. By far, the smallest errors are introduced by the BFA model. However, the present test case is particularly beneficial, since the parameter in the friction term for this model is determined and fitted for exactly this flow scenario. Thus, limiting the significance of this finding in more general flows.

Threshold for cutting at phase-field values close to zero

The numerical implementation for the application of diffuse boundary conditions requires a treatment of nodes with $\phi > 0$, which have neighbouring nodes with $\phi = 0$. The velocity of these neighbouring nodes will enter the discretisation of velocity gradients or the Laplace operator, although they are not defined. Additionally, when solving for $\boldsymbol{u}$, the phase-field function ϕ occurs in the denominator, which causes numerical problems for very small ϕ-values. Two possibilities to address these issues are found in literature. The approach used by [37, remark 2.3], and adopted in [25, 61], also considers all PDEs for $\Omega_{\phi=0}$ and uses $\phi + 10^{-6}$ with an additional threshold value to ensure well-posed-ness for small or vanishing ϕ. This yields an extension of the solution into $\Omega_{\phi=0}$, where 'far-field' boundary conditions are applied at the boundary $\partial\Omega$ of the enlarged domain Ω. According to Yu *et al* [62] this should be around $5\delta_\mathrm{d}$ away from the actual fluid solid interface. Alternatively, the approach of [49] can be used, where the PDE is only solved within $\Omega_{\phi>0}$. To do so, values are linearly extrapolated from $\Omega_{\phi>0}$ to all nodes with $\phi = 0$ and have neighbours with $\phi > 0$. Since Dirichlet boundary conditions are considered for the velocity, this approach can also be adjusted by setting $\forall\, \boldsymbol{x} \in \Omega_{\phi=0}\colon\ \boldsymbol{u} = \boldsymbol{u}^\mathrm{w}$, which is used in the present work. Instead of adding a small threshold value to ϕ everywhere, as done in [25, 37], nodes with a phase-field value below a certain threshold can be considered non-fluid, and the wall velocity is applied, preventing division by very small values. Subsequently, the influence of using such a threshold is demonstrated for the different models and interface resolutions. Furthermore, it is compared to the method with domain extension using $\phi + 10^{-6}$.

Figure 5 plots the L_2-error as a function of the number of cells $\delta_\mathrm{d}/\Delta x$ in the interface for different models. The model formulations BFA, LA2 and LA1 show an identical behaviour at different thresholds, depending on the number of cells in the solid-fluid interface. Therefore, only LA1 is shown as an example. There, it can be seen that the cutting threshold does not impact the error at all. Furthermore, the linear extrapolation and the domain extension approach differ only slightly. In contrast, the formulations that employ a direct evaluation of the Laplace operator, BDA and LDA, exhibit differences in their behaviour, in terms of the threshold. For certain interface resolutions $\delta_\mathrm{d}/\Delta x$, peaks in the L_2-error occur which are particularly observed for low thresholds and the domain extension approach. Increasing the threshold tends to diminish these peaks. It should be noted that BDA and LDA are relatively sensitive to the cutting at specific $\delta_\mathrm{d}/\Delta x$-ratios, which is not the case with the other models.

Discussion of the model and numerical errors

For the previous section, a very high numerical resolution is chosen in order to achieve negligible numerical errors and isolate the model errors. However, in practical application, such numerical resolutions are not affordable. Therefore, the effect of combined numerical and model errors is investigated subsequently. For different numerical resolutions characterised by the cell count $n = H/\Delta x$ over the channel height, simulations with varying interface width are conducted. This leads to different resolutions of the diffuse interface width, by means of the number of cells $\delta_\mathrm{d}/\Delta x$ in the interface. A larger amount of cells in the interface $\delta_\mathrm{d}/\Delta x$ leads to an increased interface thickness for a fixed overall resolution, and therefore, a better interface resolution. Two counteracting effects are expected for varying

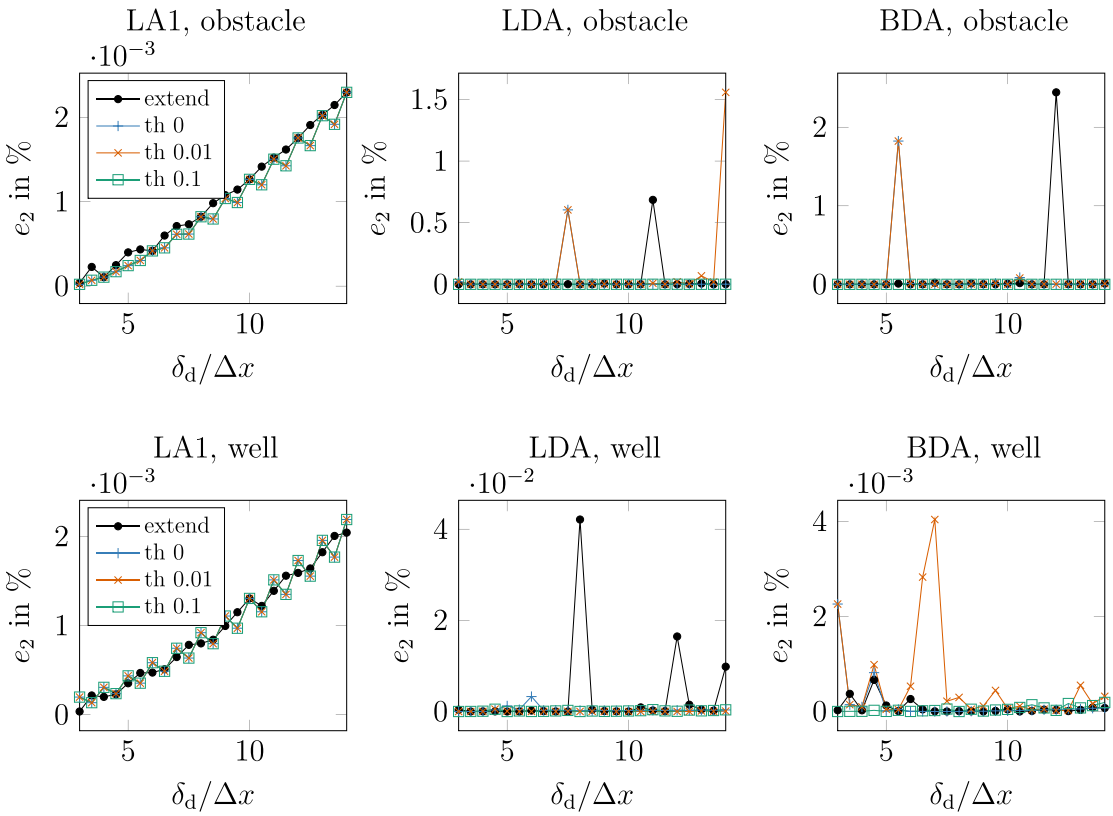

Figure 5. Influence of the cutting threshold $\in \{0, 0.1, 0.01\}$, and comparison with the domain extension (extend) method for selected models and a varying number of cells per interface ratios at a resolution of 5000 cells. The models BFA, LA2 and LA1 show no influence with regard to the choice of the cutting threshold. Therefore, BFA and LA2 are not depicted.

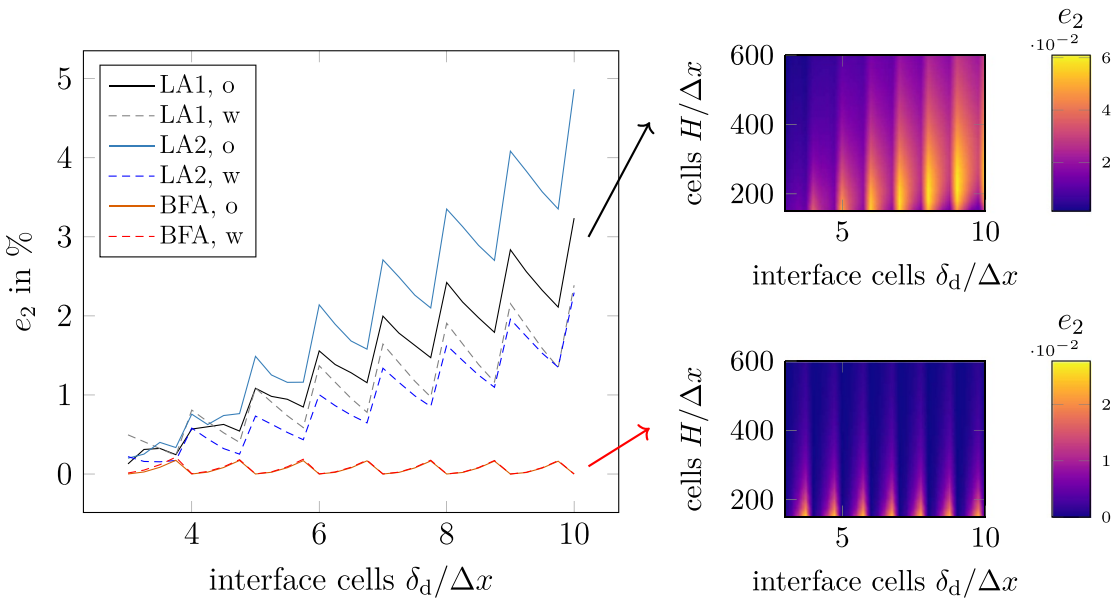

Figure 6. Errors for different interface resolutions, at fixed number of total cells, for the channel flow case. Left: L_2-error over the number of cells in the interface, calculated via $\delta_d/\Delta x$, for a fixed number of total cells $n = H/\Delta x = 600$. Right: Example of the error over the whole parameter space of total cells and interface cells, for two models (LA1 and BFA) with obstacle potential.

the number of interface cells. While numerical errors, arising from the discretisation of the phase-field profiles, decrease with higher resolution of the interface, the increased interface thickness will lead to larger model errors. Figure 6 shows the results by means of the L_2-error. Regarding the error e_{bulk}, similar patterns are observed. Thus, it is not shown. Due to space limitations, only exemplary results are shown. The full results are given as supplementary material. Firstly, it should be noted that due to numerical

errors, the overall accuracy is lower than in the case where only model errors occur. The LA2 approximation at $\delta_d = 0.01H$, for example, yields an L_2-error of 0.2% for 12 000 cells, around 1% for 600 cells and around 2.5% for 400 cells. From the plots at the right of figure 6, it can be observed, that for most models, the errors become smaller if the overall resolution is increased. Regarding the variation in interface cells, a smaller number of cells in the interface, leads to a trend of smaller errors. Only for the BFA approximation, this trend is not observed. Instead, it seems relatively insensitive to the interface resolution. In all models, the overall trend of the slopes is superimposed by a sawtooth pattern, where for $\delta_d/\Delta x$ as an integer, the error exhibits a local maximum, while it decreases again until the next integer is reached. For planar interfaces, and when the interface is grid-aligned, a similar behaviour is observed with regard to the interface free energy in phase-field models, which is discussed in detail in [52, chapter 6.2.3] for an obstacle potential. This effect can be explained by the discretisation of the $\|\nabla\phi\|$ slope depicted in figure 2. The accuracy of a numerical integral of $\|\nabla\phi\|$ over η depends significantly on how close the next grid node is to the maximum of this profile, since the difference between this maximum and the value at the node next to it is dropped. The direct approximations BDA and LDA are not depicted in figure 6, but the results may be found in the supplementary material. Compared to the other models, they exhibit significantly larger errors and produce some outliers for certain $\delta_d/\Delta x$-ratios with errors of over 100%, suggesting that there is no stable solution. This behaviour is already visible in figure 5, where the influence of the cutting value is discussed. This is consistent with the findings of Li *et al*, who conclude from their experience that direct approximation is not robust [37, sec. 2.3.1.].

Discussion of the Couette flow results

Subsequently, the results for the Couette flow for the high-resolution setup with negligible numerical errors are discussed. The errors of different diffuse approximations over the diffuse interface thickness are shown in figure 7.

Obstacle potential. For the obstacle potential, the approximations BFA, BDA and LDA, which all include the term $\boldsymbol{u}^w\nabla\cdot(\mu\nabla\phi)$, do not converge in the sharp interface limit. In contrast, they exhibit an increased error at smaller interface widths, which is a result of the upper boundary, where the wall velocity is imposed. If only the lower boundary is considered to be diffuse, a monotone convergence is observed. This indicates that imposing the wall velocity via $\boldsymbol{u}^w\nabla\cdot(\mu\nabla\phi)$ is prone to errors at small interfaces. In contrast, the approximations LA1 and LA2 yield a convergence and very small errors, which do not exceed 0.1% even at the largest considered interface width of $\delta_d = 0.2H$. These two models have no problems to impose wall velocity and also deliver much higher accuracy than in the case of Poiseuille flow. This indicates that the linearity of the velocity profile makes the Couette flow a favourable problem for these approximations.

Well potential. For the well potential, the behaviour differs significantly from the behaviour of the obstacle potential. The overall errors for the approximations BFA, BDA, and LDA are for all interface thicknesses smaller compared to the obstacle case. These models seem to work much better for the well potential, compared to the obstacle potential. The LDA model seems to converge very well until it reaches $\delta_d = 0.05H$ or below. This is in contrast to the obstacle case, where the error monotonically increased with small interface widths. The BFA approximation exhibits an almost constant error for $\delta_d > 0.02H$. In the case of smaller interface widths, the error decreases, without vanishing entirely. Regarding the BDA approximation, a convergence regarding the L_2-error is observed, which is very slow at large interface widths and accelerates at small ones. With respect to e_{bulk}, convergence is only observed for $\delta_d < 0.05H$. For all approximations, the L_2-error is two orders of magnitude smaller than the absolute value of e_{bulk}, whereas for the Poiseuille flow, there is only one order of magnitude difference between the two error measures. This points to the fact that the main part of the errors occurs in the interface $\Omega_{\phi<1}$, which is included in the e_{bulk}-error (see equation (38)) and not in the region $\Omega_{\phi=1}$ of pure fluid.

Conclusion for the Couette flow. The main finding is that the approximations LA1 and LA2 are the most convenient for the case of non-vanishing wall velocity. Moreover, the other approximations, which include the term $\boldsymbol{u}^w\nabla\cdot(\mu\nabla\phi)$, perform much worse, in particular for the obstacle potential case. In terms of the well potential, they perform better, with BFA and BDA showing convergence and LDA diverging only at very small interfaces. With regard to LDA, the author [37] already found that this

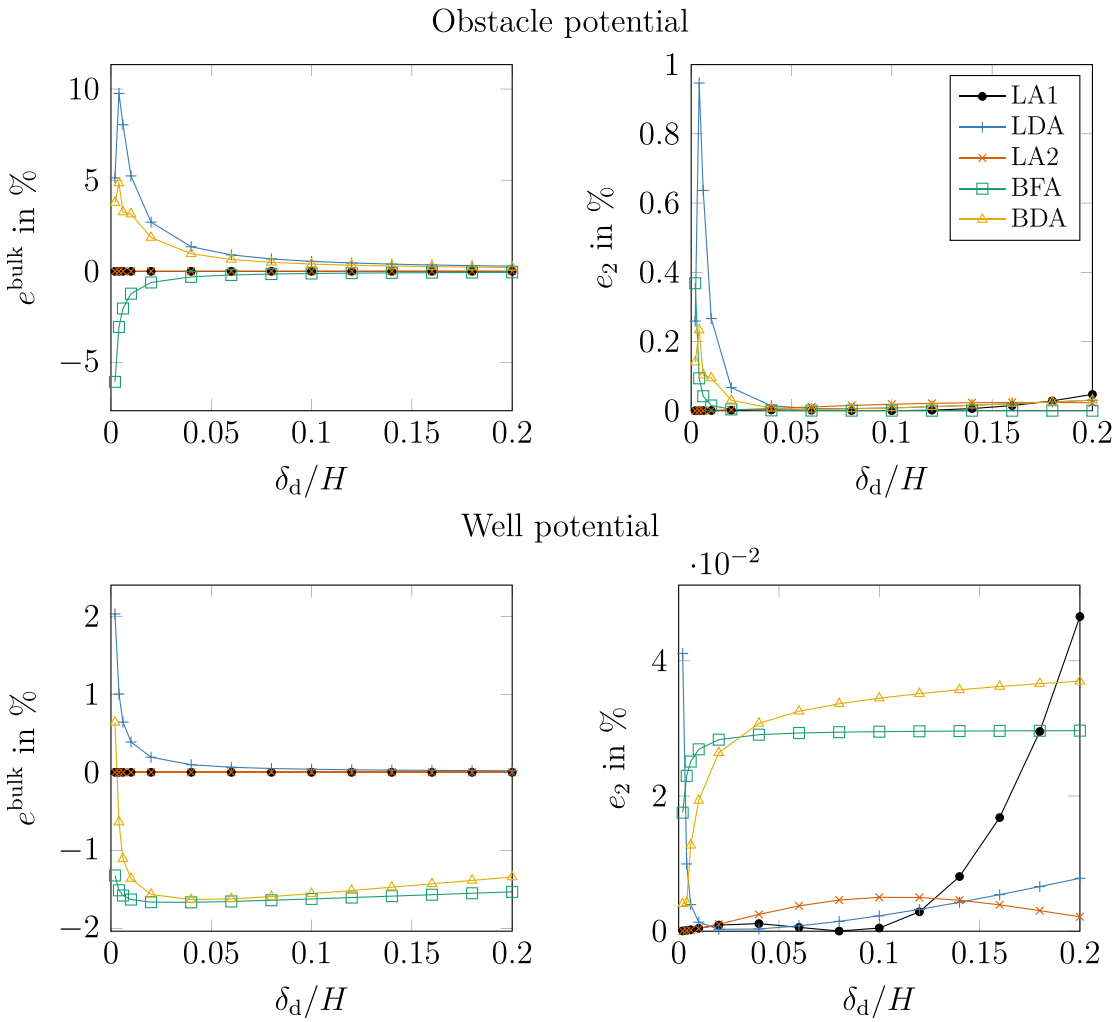

Figure 7. Model errors of the different diffuse approximations for Couette flow at various interface thicknesses. Left: Relative error $e_{\text{bulk}} = (\overline{u} - \overline{u}_{\text{ref}})/\overline{u}_{\text{ref}}$ regarding the bulk velocity $\overline{u}$, cf equation (38). Right: L_2-error regarding the velocity field, according to equation (39).

approximation is not particularly robust. In the BFA and BDA approximations, one source of inaccuracy could be that the analytical term $(\boldsymbol{u}^{\text{w}} - \boldsymbol{u})\nabla \cdot (\mu \nabla I)$ is split, with the part containing $\boldsymbol{u}^{\text{w}}$ being approximated directly with ϕ, while the part containing $\boldsymbol{u}$ is approximated differently. This inconsistency might be the source of inaccuracies if $\boldsymbol{u}^{\text{w}} \neq \boldsymbol{0}$. The fact that these approximations work better with the well potential suggests that imposing a wall velocity requires a distribution function that is more condensed around $\phi = 0.5$ (see right plot in figure 2).

Interim conclusion for both channel flow cases

The investigations for the Poiseuille and Couette flow reveal that the diffuse approximation formulations exhibit different degrees of accuracy. In both flow scenarios, the direct approximations LDA and BDA perform relatively poor and are not always robust. Therefore, they are not of great interest for the application and are not taken into account in the following studies, which are only performed for BFA, LA1 and LA2. A significant difference is observed with regard to the wall velocity. For vanishing wall velocity (Poiseuille flow), the BFA model is the most accurate one, while for imposing a wall velocity (Couette flow), it is significantly inferior to LA1 and LA2. This can be attributed to the fact that BFA was originally only introduced for $\boldsymbol{u}^{\text{w}} = \boldsymbol{0}$ and the extension to a wall velocity not equal to zero introduces different approximations for originally identical terms. Regarding these examples, using BFA for $\boldsymbol{u}^{\text{w}} = \boldsymbol{0}$ and LA1 or LA2 for $\boldsymbol{u}^{\text{w}} \neq \boldsymbol{0}$ is found to be a good choice. In these cases, there is also no significant difference between the phase-field profile of the obstacle and that of the well type. The difference between the obstacle and well profile only seems to be significant when the approach is relatively poor anyway. In these cases, the well profile yields the more accurate results. Since the subsequent studies

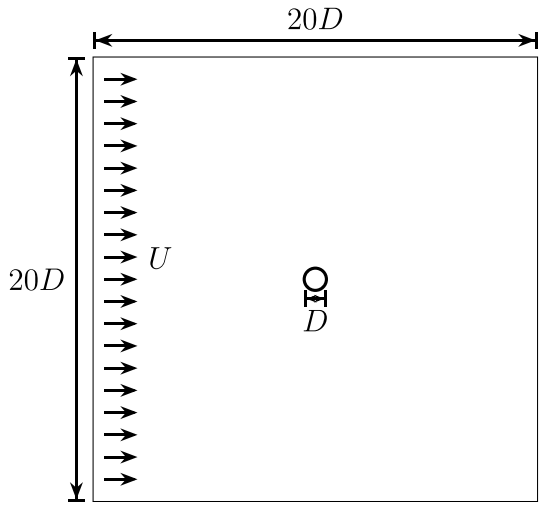

Figure 8. Sketch of a flow past a cylinder, with the inflow velocity U and the cylinder diameter D.

are restricted to the robust models BFA, LA1 and LA2, no large difference between obstacle and well is expected. Therefore, only the obstacle results are evaluated in the upcoming sections.

3.2. Flow past a cylinder (Kármán)

Reference solution and benchmark quantities

In order to compare the error of the different phase-field models with regard to the flow around a cylinder, the reference solution of Gautier *et al* [23] is used in this section. The reference solution q_{ref} is specified by the authors for a Reynolds number of $Re = \rho UD/\mu = 40$, where ρ, U, D and μ are the density, the inflow velocity, the diameter of the cylinder and the viscosity. Therefore, a low Reynolds number regime is considered, where no vortex shedding is expected and a stationary flow is established. In addition, the domain is given by $L_x \times L_y = 20D \times 20D$, with $D = 1$ in the dimensionless case. With the reference solution q_{ref}, the L_2-error for a certain scalar field $q(\boldsymbol{x})$ can be calculated according to

$$e_2(q) := \int_{\Omega_{\phi=1}} (q - q_{\text{ref}})^2 \, \mathrm{d}V \left(\int_{\Omega_{\phi=1}} (q_{\text{ref}})^2 \, \mathrm{d}V \right)^{-1}. \tag{40}$$

In the following analysis, an evaluation based on the velocity error $e_2(\|\boldsymbol{u}\|)$, which is calculated from the magnitude of the velocity $\|\boldsymbol{u}\|$, is performed. Furthermore, an analysis of the pressure error $e_2(p)$ is presented. To obtain the reference solution, it is necessary to apply the interpolation script developed by Gautier *et al* [23], which provides the reference solution for a given resolution. In this section, the influence of the models LA1, LA2 and BFA is investigated with a constant number of 6 cells in the interface in a grid refinement study. Additionally, the impact of the number of cells in the fluid–solid interface is analysed for the three distinct models.

Simulation setup

For this benchmark, a cylinder with a diameter of D is placed in a simulation box measuring $20D \times 20D$. The cylinder is located in the middle of the simulation domain. For this simulation study, a Cartesian grid with $n_x \times n_y$ cells is employed for discretisation, where $n_x = n_y = n$ is used in a range of 192 to 608, with n. A Reynolds number of $Re = 40$ is set in relation to a dimensionless density of $\rho = 1$ and a dynamic viscosity of $\mu = 1/40$. For the given set of parameters, the inflow velocity is determined to be $U = 1$, which is set as a Dirichlet boundary condition on the left side of the simulation domain. Furthermore, a pressure boundary condition is utilised on the right side, by using the reference solution from Gautier *et al* [23]. At the top and bottom wall, slip boundary conditions are used. A sketch of the simulation setup is shown in figure 8. The obstacle-type sin-profile is used for the simulations. For the subsequent two-dimensional benchmark cases, the numerical simulations are performed using the solver PACE3D [28]. For spatial discretisation, a preserving finite difference scheme using second order central differences on a Cartesian grid is employed. A staggered grid arrangement is used to avoid pressure–velocity decoupling. Therefore, the velocity components are located at the cell faces in the corresponding

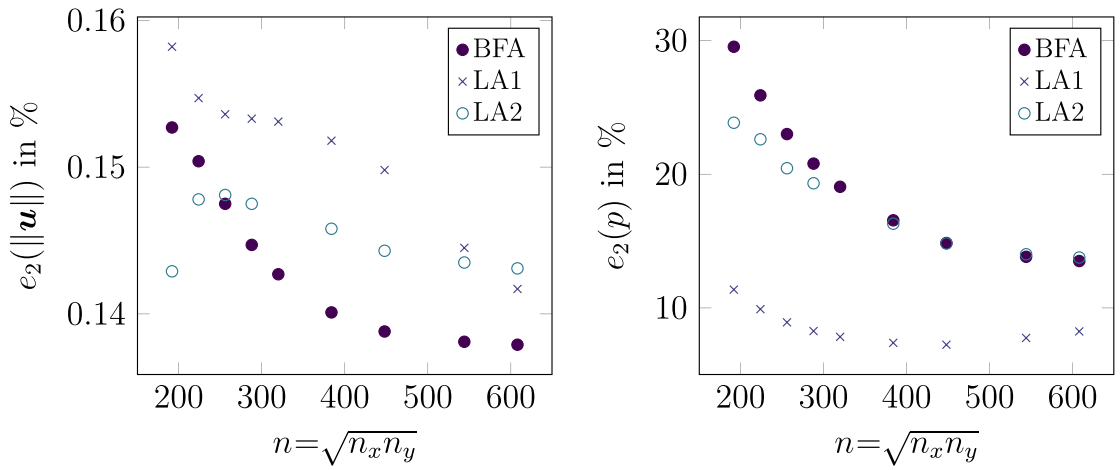

Figure 9. Velocity error $e_2(\|\boldsymbol{u}\|)$ (left) and pressure error $e_2(p)$ (right) in % for different resolutions and models according to equation (40). The different models are shown in black, red and blue for BFA, LA2 and LA1, respectively. A value of 6 cells in the fluid–solid interface is chosen.

coordinate direction, while the pressure is located at cell centres. The Navier–Stokes system is solved to stationary equilibrium with a Chorin-type projection method

Discussion of the results for different models

Figure 9 shows the errors of the velocity field $e_2(\|\boldsymbol{u}\|)$ and the pressure field $e_2(p)$ in % as a function of the resolution.

The velocity error $e_2(\|\boldsymbol{u}\|)$ is illustrated on the left in figure 9. For the three distinct phase-field models, the same behaviour is evident in the global scenario. As the resolution increases, the error in the velocity field decreases. As expected, a monotonically decreasing convergence is only observed for the models BFA and LA1. For the model LA2, it can be seen that this behaviour is valid from a resolution of $n = 256$, which suggests that the two smallest resolutions are not within the convergence radius for the model LA2. Disregarding these two data points of LA2, the BFA model yields the smallest errors with respect to the velocity. Overall, with a maximum value of 0.1547%, all models show a small relative error for all given resolutions. The error $e_2(p)$ in the pressure field is shown on the right in figure 9. For the models BFA and LA2, the pressure error shows a monotonically decreasing trend with increasing resolution. In contrast, the LA1 model shows a slight increase for the two finest resolutions after a monotonically decreasing error for $n < 500$. However, the error of the LA1 model is the smallest at all resolutions, which is not the case for the velocity error. Compared to the other two models, LA2 produces smaller errors up to $n \approx 488$, while they produce very similar errors, with BFA having a slight advantage over LA2 at finer resolutions. Notably, the relative errors of the pressure are generally much higher, compared to the velocity errors. Furthermore, considering both errors, no clear trend is observed. While LA1 yields the smallest pressure errors, its velocity errors are larger than the ones for the other models. In summary, it can be concluded that all three models are capable of representing the flow around a cylinder for $Re = 40$. The evaluation of the error, using the provided reference solution, allows a comparison of the different models and can be used for future model formulations. Furthermore, the model formulations demonstrate the expected behaviour in the event of an error in the velocity field with acceptable errors in terms of accuracy, provided that the resolution is not too poor, i.e. above $n = 288$. As far as pressure is concerned, the errors in all models are relatively large. Overall, the errors of all models are of a similar magnitude, and no clear trend can be observed, which means that no model is clearly superior in terms of the final state.

Discussion of the results for the amount of interface cells

The impact of the number of cells $\delta_d/\Delta x$ in the fluid–solid interface is subsequently investigated for a resolution of $n = 224$. Increasing $\delta_d/\Delta x$ leads to both a higher resolution of the diffuse interface and, at the same time, a larger interface width. In figure 10, the corresponding results are shown.

A different behaviour in the velocity error $e_2(\|\boldsymbol{u}\|)$, which is presented on the left side of the figure, can be observed for the different models. The LA1 model exhibits a monotonically increasing error for

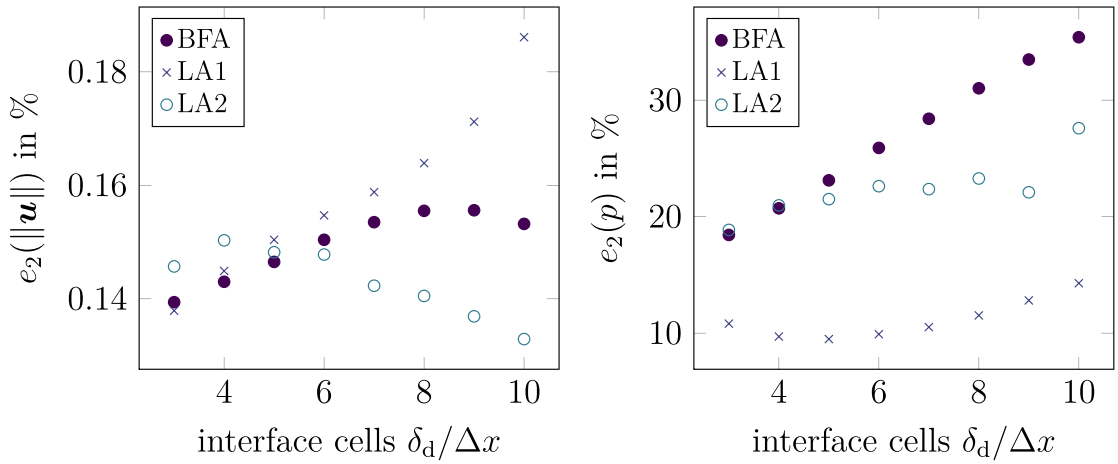

Figure 10. Velocity error $e_2(\|\boldsymbol{u}\|)$ (left) and pressure error $e_2(p)$ (right) in % for the distinct models in relation to the cells in the fluid–solid interface. The resolution is set to $n=\sqrt{n_x n_y} = 224$.

an increasing number of cells in the interface. This indicates that modelling errors increase more significantly, due to the larger interface, than the error reduction, due to the better resolution of the phase-field profile. In contrast, for the BFA and LA2 models, the error increases only up to a certain amount of cells in the fluid–solid interface, after which they fall again. These numbers are 4 and 9 cells for the LA2 and BFA models, respectively. With regard to the pressure error, all three models show the same trend, namely that the error increases with a larger interface. For the LA1 model, the lowest values are an exception, as the error initially decreases before increasing again from a value of 5 cells. Compared to the results in figure 6, where the influence of $\delta_d/\Delta x$ is investigated for the channel flow, no sawtooth pattern is observed. This is due to the fact that a curved interface is considered, which does not align with the grid. Therefore, the distribution of grid nodes in the normal direction of the interface differs at different points on the surface of the cylinder.

Interim conclusion for the flow past a cylinder

Regarding this benchmark, various conclusion can be drawn. The velocity errors for the various models, resolutions and cells in the interface are only minor, which is not the case with the pressure error. Especially, if we compare the BFA model results from this benchmark case with the results of both channel flows, it performs significantly poorer. This is due to the fact that the friction coefficient in this model is particularly fitted to match the channel flow case. However, for the cylinder flow, the regime of a linear velocity gradient near the wall is very small, and therefore, the assumptions of the BFA model are not met, as well as for the channel flow case. Furthermore, varying the number of cells in the interface with a fixed overall resolution leads to different results when comparing the cylinder flow with the channel flow. For the latter, a sawtooth pattern is observed (cf figure 6), which does not occur for the cylinder flow (figure 10). Additionally, the interface resolution shows that a greater interface thickness at a fixed resolution tends to lead to an increase in errors. While this trend is clearly visible for the channel flow, it only partially applies to the flow past a cylinder. It seems that in the case of flow past a cylinder, the models respond differently to variations in the number of interface cells, reflecting the increased complexity of a curved surface, compared to a planar surface.

3.3. Boundary layer flow

Analytic solution and benchmark quantities

The next benchmark case considers boundary layer flow. Let u denote the velocity component tangential to the wall, x and y the wall tangential and normal coordinate, respectively, $U = \lim_{y\to\infty} u$ the outer flow velocity and $Re_x := \rho U x/\mu$. Important measures of the boundary layer are the displacement thickness δ_1, momentum thickness δ_2 and energy thickness δ_3, defined as

$$\delta_1 = \int_0^\infty 1 - \frac{u}{U}\,\mathrm{d}y, \quad \delta_2 = \int_0^\infty \left(1 - \frac{u}{U}\right)\frac{u}{U}\,\mathrm{d}y, \quad \delta_3 = \int_0^\infty \left(1 - \frac{u^2}{U^2}\right)\frac{u}{U}\,\mathrm{d}y, \tag{41}$$

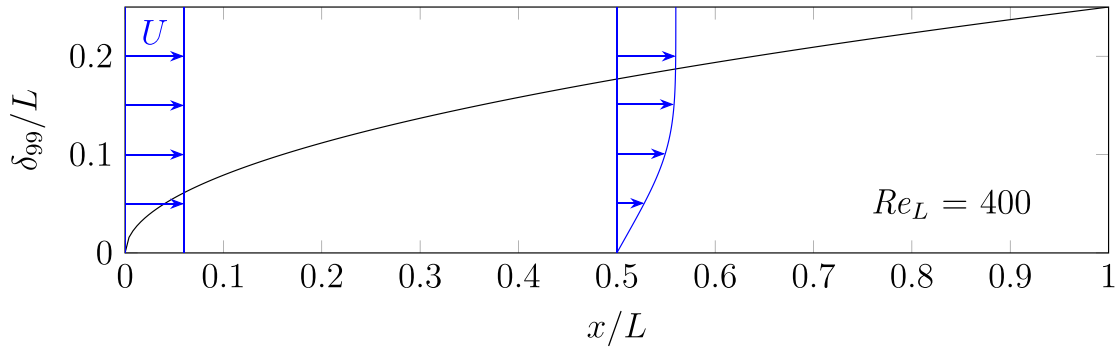

Figure 11. Sketch of a boundary layer formed by a flow over a flat plate, based on the Blasius solution, shown for a segment of length L, with the Reynolds number $Re_L = \rho UL/\mu = 400$. Blue: velocity profiles at $x = 0$ and $x = L/2$. Black: boundary layer thickness δ_{99}, where $u(\delta_{99}) = 0.99U$ holds.

respectively. For a flat plate, the well-known Blasius similarity solution [7], based on the Prandtl boundary layer equations, can be used as reference, which yields

$$\delta_1 = 1.7208\sqrt{\frac{\mu x}{\rho U}}, \quad \delta_2 = 0.664\sqrt{\frac{\mu x}{\rho U}}, \quad \delta_3 = 1.0444\sqrt{\frac{\mu x}{\rho U}}. \tag{42}$$

From this, the L_2-error can be calculated for the three different measurements, according to equation

$$e_2(q) := \int_0^L (q - q_{\text{ref}})^2 \, \mathrm{d}x \left(\int_0^L (q_{\text{ref}})^2 \, \mathrm{d}x \right)^{-1}. \tag{43}$$

Simulation setup

A sketch of the simulation setup can be seen in figure 11. A boundary layer with the Reynolds number $Re_L = 400$ and the domain $L \times 0.2L$ is considered. The choice of the Reynolds number $Re_L = 400$ is made to cover a problem with larger Reynolds number compared to the previous benchmark case of the cylinder flow. The discretisation is done with $n_x \times 2/3\, n_x$ cells, where different refinements for n_x are considered. As in section 3.1, the domain on the lower side is extended by half the diffuse interface width to ensure that the 0.5 iso-line of the phase field lies at $y = 0$, and the obstacle profile of type sin is used. On the left side, a Dirichlet boundary condition is used with a value of $\boldsymbol{u}(x = 0, y) = U\boldsymbol{e}_x$. At the top boundary, the velocity is prescribed using a Dirichlet boundary condition of the velocity from theory, i.e. $\boldsymbol{u}_{\text{top}} = U\boldsymbol{e}_x + V\boldsymbol{e}_y$, with

$$V = 1.2165\sqrt{\frac{\mu U}{2\rho x}}. \tag{44}$$

Details can be found in the appendix A.4.

Discussion of the results

Figure 12 shows the results for the given problem. In the top row, the L_2-errors for the different benchmark quantities and models are shown as a function of the resolution. Furthermore, the middle row compares the distinct quantities with the analytical solution, according to the Blasius solution, while in the last row, the numerical solution for different resolutions is compared with the Blasius solution for the BFA model.

Displacement thickness. With regard to δ_1, a decreasing error for an increasing resolution can be observed for all models, while the errors are the same for all three models. This can also be seen when the displacement thickness (δ_1/L) is plotted against the length (x/L) of the problem and compared with the analytical solution. The displacement thickness δ_1 is a measure of the loss of volume flow in x-direction, compared to the free flow. Since the volume flow rate is prescribed at the left and top boundary by velocity boundary conditions, the fact that δ_1 coincides with all models indicates that they all fulfil mass conservation and do not induce an artificial inflow velocity at the bottom. From this, it can be concluded for this benchmark quantity that the models have no influence on the mass conversion, according to the displacement thickness δ_1. Furthermore, a convergence of the error can be seen both in

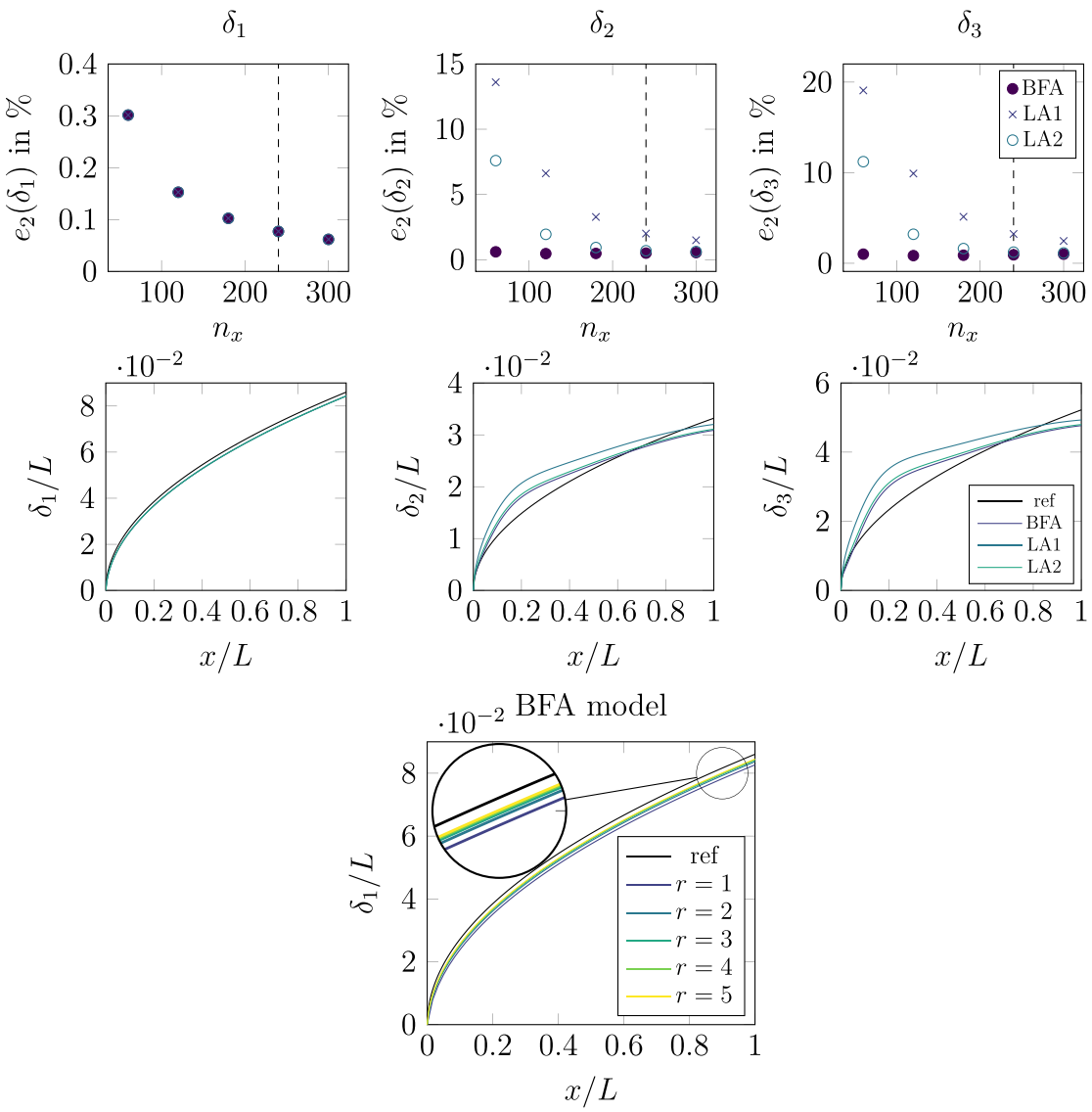

Figure 12. Different L_2-errors for the distinct models (top) and the corresponding boundary layers, at a resolution of $n_x = 240$ (vertical dashed lines in the top row), compared to the reference (middle). A grid refinement study with $n_x = 60r$ cells and refinement factors $r \in \{1, 2, 3, 4, 5\}$ for the BFA model is shown for δ_1 (bottom).

the error and in the displacement thickness itself. The latter is plotted in the bottom row of figure 12, where the numerical solutions for different resolutions are displayed against the Blasius solution. It can be seen that, for a grid refinement, the numerical solution agrees better with the analytical solution, while the individual models generally show good agreement with the analytical solution. This is also indicated by the small L_2-errors from the first image, which are below 0.3% for the given resolutions.

Momentum and energy thickness. In contrast to the behaviour for δ_1, the errors for the two other benchmark quantities δ_2 and δ_3 are different for the three models. As can be seen in the first row and the second and third column of figure 12, the relative errors for δ_2 and δ_3 show a decrease with increasing resolution for the models LA1 and LA2. In contrast, the BFA model exhibits nearly constant errors of around 2% for all resolutions, which is the lowest of all models. Both the LA1 model and the LA2 model exhibit a higher relative error for all resolutions in all cases, with LA1 delivering the highest error values for all resolutions. At higher resolutions, starting at $n_x = 240$, the relative errors for the LA2 and BFA models are almost identical. Comparing the two different thicknesses δ_2 and δ_3 over the length (x/L), the same behaviour can be observed for all three models. They cut the Blasius solution at a certain distance from the beginning $(x = 0)$. This distance increases for the models BFA, LA2 and LA1. Before this distance, all models overestimate the Blasius solution, while they underestimate the solution after this point. One possible reason for the overestimation may be the singularity at $x = 0$ due to

the simulation setup, while the underestimation can be explained by the edge of the far field, as this is probably not far enough away. Another notable point is the large difference between the distinct errors. For the δ_1-errors, the value is below 0.3%, while the error for δ_2 and δ_3 is above 1% up to 20% for δ_3 at the coarse grid refinement. The reason for this lies in the definition of the different thicknesses. For the displacement thickness, only the value of the velocity u relative to the inflow velocity is taken into account, while for the other two errors, the second and third powers of this value occur. Therefore, the same deviation in the velocity profile u leads to larger errors in momentum thickness and energy thickness, as these are amplified by the squared and cubic velocities. As a concluding remark on boundary layer flow without suction, it can be said that all models show good agreement with the Blasius solution, if the resolution is high enough. In particular, the BFA model has the lowest error values.

Boundary layer with uniform suction

Reference solution. For a boundary layer flow employing uniform suction at the lower wall, with a velocity $v_w \leqslant 0$, a reference solution is given by [30], based on a similarity solution of the boundary layer equations. This similarity solution is obtained by adjusting the boundary conditions for suction or blowing cf, e.g., [38]. More details are given in appendix A.4. The reference solution for the thickness measures is obtained by the similarity solution, which is calculated by the solver script provided as supplementary material. The evaluation equation (43) is used for the error with this reference solution.

Simulation setup. The simulation setup is similar to the one without suction, with two exceptions. Instead of using equation (44) to prescribe the theoretical boundary conditions at the top, a more complex x-dependence for the displacement velocity results, which can be evaluated using a script provided as supplementary material. Furthermore, a fixed value for the wall velocity $v_w = -0.02U$ is set at the bottom of the simulation domain. The results of this study are presented in figure 13. The top row shows the L_2-errors for the individual boundary layers at different resolutions. Furthermore, the dashed black lines in each error plot indicate the resolution ($n_x = 240$) for the second row, which illustrates the resolution of the boundary layers, denoted by δ_1/L, δ_2/L and δ_3/L, in relation to the length (x/L). The bottom row of the figure shows the boundary layer thickness δ_1 of the BFA model for varying resolutions. For the figures illustrating the various boundary layer thicknesses, the reference solution from the script is depicted in black.

Global errors at different resolutions. The L_2-error for the displacement thickness δ_1 is again the same for all models. From approximately 2.5% upwards, errors decrease monotonically at higher resolutions, reaching a final value of around 1.4%. This behaviour can also be seen in the bottom row of figure 13, where the curve of the reference solution is better approximated at higher resolution. It is reasonable to expect such behaviour, given that numerical inaccuracies are reduced with enhanced resolution. A comparison with the results without suction reveals that the error values regarding δ_1 are approximately ten times higher for the displacement thickness. A different behaviour is present for the momentum thickness δ_2. In the absence of suction, all three models converge to minor errors, with the BFA model in particular exhibiting a minimal error across all resolutions. In the case of suction, the magnitude of the error is approximately 20 times larger. In the BFA model, this error converges from the coarsest to the finest resolution, from approximately 8.56% to 7.38%. Compared to the other models, the BFA model demonstrates the poorest performance, with the exception of the lowest resolution ($n_x = 60$). At this resolution, the LA1 model demonstrates suboptimal results, exhibiting an error rate of 12.02%. Furthermore, the LA1 does not demonstrate a monotonically decreasing error with increasing resolution. For the finest resolution the error is 3.05%, which is higher than the minimal error of 2.18% arising at a resolution of $n_x = 180$ cells. A similar trend is exhibited by the model LA2. Compared to the model LA1, this model is worse for all cases with a resolution greater than $n_x = 120$. The same overall behaviour is observed for the error in the energy thickness δ_3, although the errors are generally larger than for the momentum thickness.

Distribution of deviation over the run length. For the boundary displacement thickness, the reference solution is well matched for smaller run lengths x. With larger run lengths, the deviation from the reference solution increases, indicating that the suction of the boundary condition is overestimated. Regarding the course of δ_2 and δ_3 over x, a similar behaviour compared to the case without suction is observed in even more pronounced fashion. At first, there is an overshoot followed by a kink in the course of the thickness curves. After an intersection point with the reference solution, an

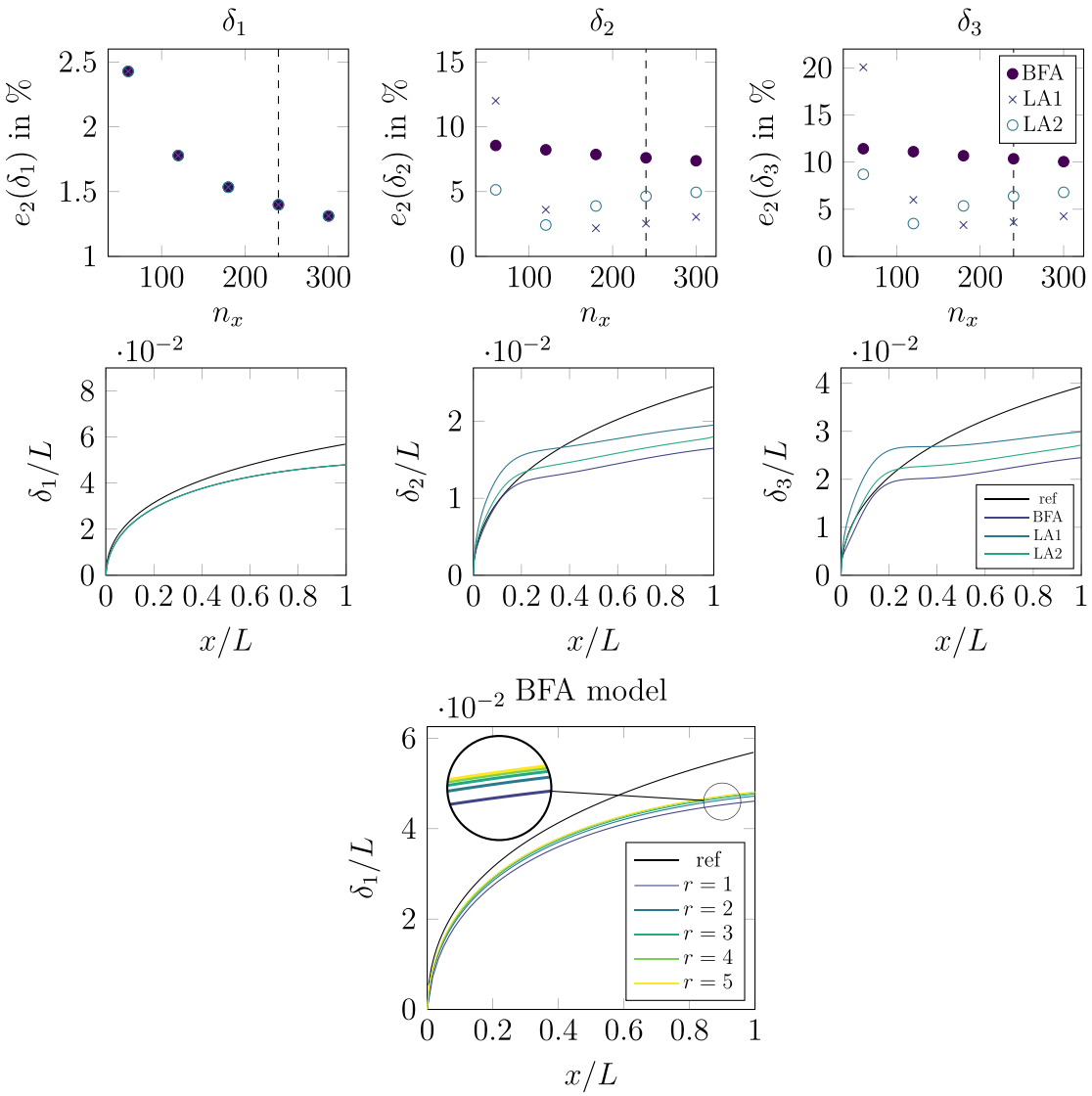

Figure 13. Different L_2-errors for the distinct models (top) and the corresponding boundary layers at a resolution of $n_x = 240$ (middle), which is indicated by the vertically dashed line in the top-row plots. A study on grid refinement for the BFA model is shown for δ_1 (below). The boundary condition is set to $v_w = -0.02U$.

underestimation further downstream can be observed. This intersection point is first reached for BFA, then for LA2 and LA1. In all models, this occurs further upstream, compared to the case without suction. While the reason for the course of δ_2 and δ_3 is the same as in the case of $v_w = 0$, the amplification of these trends may be attributed to an overestimation of the suction velocity by the different models.

Conclusion for the suction case. In summary, it can be said that in the case of suction at the lower boundary of the simulation domain, the errors of all models are significantly larger than in the case without suction. In particular, it is noticeable that the BFA model performs significantly worse for $v_w \neq 0$, compared to $v_w = 0$. Since a similar observation is made for the Couette flow, this points towards BFA being relatively inaccurate in the presence of a non-vanishing wall velocity. A reason may be the fitting of the wall friction parameter, which is adapted to a flow that does not incorporate a velocity at the boundary.

4. Concluding remarks

In this work, different existing approaches to apply velocity boundary conditions in the diffuse interface of a phase-field model are reviewed, and a quantitative comparison of the different models is made. A theoretical discussion of the various models is provided, whereby the BFA model [5] is generalised

to include a wall velocity unequal to zero. For a quantitative assessment, several benchmarks are introduced, where reference or analytical solutions are provided. The present study uses the benchmark cases to facilitate a comprehensive discussion of the influence of numerical resolution, model formulations, interface widths and distinct phase-field profiles. The studies show varying degrees of accuracy and convergence behaviour among the models and demonstrate that the model is most accurate when wall velocity changes are taken into account.

The channel flow cases show that both the direct approximations LDA and BDA perform worse than the other models. In particular, instabilities occur for Poiseuille flow at certain interface resolutions, and no convergence or only poor convergence is observed for Couette flow. Therefore, these models are not feasible for practical use. With respect to these two channel flow problems, the BFA model is the optimal selection in the scenario where no wall velocity is prescribed at the interface, i.e. $\boldsymbol{u}^{\mathrm{w}} = \mathbf{0}$. Conversely, if $\boldsymbol{u}^{\mathrm{w}} \neq \mathbf{0}$, BFA is relatively inaccurate, while LA1 and LA2 are the most suitable models. This finding is confirmed for the boundary layer flow, in presence and absence of suction. For more complicated setups, the differences between the LA1, BFA and LA2 models become less severe, which is observed by comparing the cylinder and Poiseuille flow benchmark. Furthermore, diffusively prescribing a tangential boundary velocity is more feasible, compared to a normal wall velocity (blowing/suction), where all diffuse models are relatively inaccurate. A substantial impact of the diverse phase-field profile is only evident for setups where specific models demonstrate instabilities or lack of convergence, which makes them not feasible for the given problem. Whenever convergence is observed, the trends for well- and obstacle-type profiles are identical. The studies in which the interface width is varied at constant numerical resolution show that, when applying the diffuse boundary condition, a smaller but less resolved diffuse interface tends to provide higher accuracy, compared to a larger but better resolved interface. This trend is very clear in the case of the planar interface, whereas there are exceptions to this trend in the case of cylindrical flow. In summary, the findings of this work suggest that the direct approximations LDA and BDA are not feasible for practically relevant numerical resolutions. The BFA model is the optimal choice whenever a zero wall velocity is considered, while for a non-zero wall velocity, LA1 or LA2 are preferable choices. In future studies, the combination of the benchmark with solid-fluid interfaces and other transport equations, such as the transport of temperature, can be investigated.

Data availability statement

The matlab/GNU octave code used for the channel flow benchmark as well as for the reference solution of the boundary layer flow are provided as supplementary material. Furthermore, raw data of the plots as well as additional data is provided as supplementary material. Further data that support the findings of this study are available from the corresponding author upon reasonable request. The used simulation software PACE3D is commercially available.

All data that support the findings of this study are included within the article (and any supplementary files).

Acknowledgments

The authors gratefully acknowledge financial support by the *Bundesministerium für Bildung und Forschung* (BMBF) within the KMU-innovative project BioSorb. This work contributes to the research performed at KIT excellence strategy ExU-Future Fields Stage 3 'Kadi4Mat' and Stage 2 'ACDC', which is gratefully acknowledged. In addition, financial support by the 'Materials Science and Engineering (MSE)' programme No. 43.31.01, supported by the Helmholtz association is gratefully acknowledged. It further contributes to the research performed at CELEST (Center for Electrochemical Energy Storage Ulm-Karlsruhe). The work was funded by the German Research Foundation (DFG) under Project ID 390874152 (POLiS Cluster of Excellence). Support regarding the benchmark implementation is provided through funding by the Helmholtz association within the programme 'MTET', No. 38.02.01, which is gratefully acknowledged.

Declaration of Generative AI and AI-assisted technologies in the writing process

The authors used DeepL (DeepL SE) and ChatGPT (OpenAI) to improve linguistics. All tool-assisted text was subsequently reviewed and edited by the authors, who take full responsibility for the final content of the publication.

Author contributions

Martin Reder 0000-0002-7503-9351
Conceptualization (lead), Investigation (equal), Methodology (equal), Software (supporting), Validation (supporting), Visualization (equal), Writing – original draft (equal), Writing – review & editing (supporting)

Marcel Weichel 0000-0003-2426-2665
Investigation (equal), Methodology (equal), Software (lead), Validation (lead), Visualization (equal), Writing – original draft (equal), Writing – review & editing (supporting)

Britta Nestler
Funding acquisition (equal), Writing – review & editing (supporting)

Daniel Schneider
Funding acquisition (equal), Writing – review & editing (supporting)

Appendix. Derivation of the whole domain formulation

This section shows the derivation of the whole domain Navier–Stokes equation system for the fluid–solid problem. To this end, the general procedure of Li *et al* [37] is applied both on mass balance and the Navier–Stokes equation.

A.1. Whole domain formulation of the mass balance

Considering no mass diffusion and production, the mass balance reads

$$\frac{\partial \rho}{\partial t} + \nabla \cdot (\rho \boldsymbol{u}) = 0. \tag{45}$$

Multiplication with the scalar test function ψ and integration over the fluid domain Ω_f yields

$$\int_{\Omega_\mathrm{f}} \left[\frac{\partial \rho}{\partial t} + \nabla \cdot (\rho \boldsymbol{u}) \right] \psi \, \mathrm{d}V = 0 \tag{46}$$

which is reformulated to the weak form of the mass balance

$$\int_{\Omega_\mathrm{f}} \left[\psi \frac{\partial \rho}{\partial t} - \rho \boldsymbol{u} \cdot \nabla \psi \right] \mathrm{d}V + \int_{\Gamma_\mathrm{fs}} \left[\rho \psi \boldsymbol{u}^\mathrm{w} \cdot \boldsymbol{n} \right] \mathrm{d}S = 0 \tag{47}$$

exploiting $\psi \nabla \cdot (\rho \boldsymbol{u}) = \nabla \cdot (\psi \rho \boldsymbol{u}) - \rho \boldsymbol{u} \cdot \nabla \psi$ and the Gauss divergence theorem. Using the indicator function, the volume integral can be extended from $\Omega_\mathrm{f} \subset \Omega$ to the larger domain Ω. Additionally, the localisation property of the surface Dirac distribution δ_Γ can be exploited to extend the surface integral over the domain. This gives rise to the identities

$$\int_{\Omega_\mathrm{f}} (\cdot) \, \mathrm{d}V = \int_{\Omega} I (\cdot) \, \mathrm{d}V \quad \text{and} \quad \int_{\Gamma_\mathrm{fs}} (\cdot) \, \mathrm{d}S = \int_{\Omega} \delta_\Gamma (\cdot) \, \mathrm{d}V, \tag{48}$$

and thus,

$$\int_{\Omega} \left[\psi I \frac{\partial \rho}{\partial t} - I \rho \boldsymbol{u} \cdot \nabla \psi + \delta_\Gamma \rho \psi \boldsymbol{u}^\mathrm{w} \cdot \boldsymbol{n} \right] \mathrm{d}V = 0. \tag{49}$$

With the product rule $I \rho \boldsymbol{u} \cdot \nabla \psi = \nabla \cdot (I \rho \boldsymbol{u} \psi) - \psi \nabla \cdot (I \rho \boldsymbol{u})$ holds. Additionally, the gradient of the indicator function yields $\nabla I = -\delta_\Gamma \boldsymbol{n}$. With this, equation (49) becomes

$$\int_{\Omega} \psi \left[I \frac{\partial \rho}{\partial t} + \nabla \cdot (I \rho \boldsymbol{u}) - \rho \boldsymbol{u}^\mathrm{w} \cdot \nabla I \right] \mathrm{d}V + \int_{\partial \Omega} \left[\rho \psi I \boldsymbol{u} \cdot \boldsymbol{n} \right] \mathrm{d}S = 0. \tag{50}$$

According to the fundamental lemma of variational calculus, equation (50) is only fulfilled for any test function ψ if

$$I \frac{\partial \rho}{\partial t} + \nabla \cdot (I \rho \boldsymbol{u}) - \rho \boldsymbol{u}^\mathrm{w} \cdot \nabla I = 0, \tag{51}$$

which is the whole domain mass balance. For incompressible flow, this reduces to

$$\nabla \cdot (I\boldsymbol{u}) - \boldsymbol{u}^{\mathrm{w}} \cdot \nabla I = 0. \tag{52}$$

At the boundary, equation (50) requires $\rho\psi I\boldsymbol{u} \cdot \boldsymbol{n} = 0$, which is fulfilled by $I = 0$ if no fluid is present. For the parts of the boundary with $\partial\Omega \cap \partial\Omega_{\mathrm{f}}$, it requires $\rho\psi\, \boldsymbol{u} \cdot \boldsymbol{n} = 0$ which is the same condition arising also from the weak form (47) of the fluid domain Ω_{f} and, therefore, reflects the same boundary conditions as the boundary value problem without domain extension for these parts.

A.2. Whole domain formulation of the Navier–Stokes equation

Similarly to the whole domain formulation of the mass balance, the whole domain Navier–Stokes equation can be derived. A test function $\boldsymbol{w} \in H^3_{\mathrm{D}}$ of the three dimensional Sobolew function space $H^3_{\mathrm{D}} = \{\boldsymbol{w} \in H^3(\Omega) : \quad \forall\, \boldsymbol{x} \in \partial\Omega[\mathrm{D}] : \ \boldsymbol{w} = \boldsymbol{0}\}$ is introduced, which vanished at parts $\partial\Omega[\mathrm{D}] \subseteq \partial\Omega_{\mathrm{f}}$ of the boundary where Dirichlet boundary conditions are applied. A scalar multiplication of this test function $\boldsymbol{w}$ with the Navier–Stokes equation (1*a*) and integration over the fluid domain yields the following for the viscous term:

$$\int_{\Omega_{\mathrm{f}}} [\nabla \cdot (\mu\nabla\boldsymbol{u}) \cdot \boldsymbol{w}]\ \mathrm{d}V. \tag{53}$$

To perform a two times partial integration of this term, it is exploited in such a way that the integrant can be rewritten as

$$\begin{aligned} \nabla \cdot (\mu\nabla\boldsymbol{u}) \cdot \boldsymbol{w} &= \nabla \cdot \left(\mu \left(\nabla^{\top}\boldsymbol{u}\right) \boldsymbol{w}\right) - \mu\nabla\boldsymbol{u} \cdot \nabla\boldsymbol{w} \\ &= \nabla \cdot \left(\mu \left(\nabla^{\top}\boldsymbol{u}\right) \boldsymbol{w}\right) - \left[\nabla \cdot \left(\mu \left(\nabla^{\top}\boldsymbol{w}\right) \boldsymbol{u}\right) - \boldsymbol{u} \cdot \nabla \cdot (\mu\nabla\boldsymbol{w})\right] \end{aligned} \tag{54}$$

and subsequently the Gauss divergence theorem is applied. This yields

$$\begin{aligned} \int_{\Omega_{\mathrm{f}}} [\nabla \cdot (\mu\nabla\boldsymbol{u}) \cdot \boldsymbol{w}]\ \mathrm{d}V = &\int_{\Omega_{\mathrm{f}}} [\boldsymbol{u} \cdot \nabla \cdot (\mu\nabla\boldsymbol{w})]\ \mathrm{d}V \\ &+ \int_{\Gamma_{\mathrm{fs}}} \left[\mu\boldsymbol{w} \cdot \left(\nabla^{\top}\boldsymbol{u}\right)\boldsymbol{n} - \mu\boldsymbol{u} \cdot \left(\nabla^{\top}\boldsymbol{w}\right)\boldsymbol{n}\right]\ \mathrm{d}S \end{aligned} \tag{55}$$

where $\boldsymbol{u}(\boldsymbol{x}, t) = \boldsymbol{u}^{\mathrm{w}}(\boldsymbol{x}, t)$, $\boldsymbol{x} \in \Gamma_{\mathrm{fs}}$ holds at the walls. An extension of the integrals, according to equation (48), allows to rewrite the weak form of the viscous term to

$$\int_{\Omega} [I\boldsymbol{u} \cdot \nabla \cdot (\mu\nabla\boldsymbol{w}) - \mu\boldsymbol{w} \cdot (\nabla\boldsymbol{u})\nabla I + \boldsymbol{u}^{\mathrm{w}} \cdot \mu(\nabla\boldsymbol{w})\nabla I]\ \mathrm{d}V. \tag{56}$$

These terms can be reformulated using the product rule. For the last summand

$$\boldsymbol{u}^{\mathrm{w}} \cdot \mu(\nabla\boldsymbol{w})\nabla I = \nabla \cdot (\mu\boldsymbol{w} \cdot \boldsymbol{u}^{\mathrm{w}}\nabla I) - \boldsymbol{u}^{\mathrm{w}} \cdot \boldsymbol{w}\nabla \cdot (\mu\nabla I)$$

holds. Regarding the first term of equation (56), intermediate calculations are given in index notation using Einsteins summation convention for sake of convenience. Thereby, a summation over indices arising twice is done. This gives rise to

$$\begin{aligned} I\boldsymbol{u} \cdot \nabla \cdot (\mu\nabla\boldsymbol{w}) =& Iu_i \frac{\partial}{\partial x_j}\left(\mu\frac{\partial w_i}{\partial x_j}\right) \\ =& \frac{\partial}{\partial x_j}\left(Iu_i\mu\frac{\partial w_i}{\partial x_j}\right) - I\mu\frac{\partial w_i}{\partial x_j}\frac{\partial u_i}{\partial x_j} - \mu u_i\frac{\partial w_i}{\partial x_j}\frac{\partial I}{\partial x_j} \\ =& \frac{\partial}{\partial x_j}\left(Iu_i\mu\frac{\partial w_i}{\partial x_j}\right) - \frac{\partial}{\partial x_j}\left(I\mu\frac{\partial u_i}{\partial x_j}w_i\right) + w_i\frac{\partial}{\partial x_j}\left(I\mu\frac{\partial u_i}{\partial x_j}\right) \\ & - \frac{\partial}{\partial x_j}\left(\mu u_i w_i\frac{\partial I}{\partial x_j}\right) + w_i\frac{\partial}{\partial x_j}\left(\mu u_i\frac{\partial I}{\partial x_j}\right) \\ =& \nabla \cdot \left(I\mu\left(\nabla^{\top}\boldsymbol{w}\right)\boldsymbol{u} - I\mu\left(\nabla^{\top}\boldsymbol{u}\right)\boldsymbol{w} - \mu\boldsymbol{u} \cdot \boldsymbol{w}\nabla I\right) \\ & + \boldsymbol{w} \cdot \nabla \cdot (I\mu\nabla\boldsymbol{u}) + \boldsymbol{w} \cdot \mu\left(\nabla\boldsymbol{u}\right)\nabla I + \boldsymbol{w} \cdot \boldsymbol{u}\nabla \cdot (\mu\nabla I)\,. \end{aligned}$$

Therefore, equation (56) yields

$$\int_{\Omega} \boldsymbol{w} \cdot [\nabla \cdot (I\mu\nabla\boldsymbol{u}) + (\boldsymbol{u} - \boldsymbol{u}^{\mathrm{w}})\nabla \cdot (\mu\nabla I)]\ \mathrm{d}V$$

$$+\int_{\partial\Omega}\mu\boldsymbol{w}\cdot(\boldsymbol{u}^{\mathrm{w}}-\boldsymbol{u})\nabla I\cdot\boldsymbol{n}+I\left(\mu\left(\nabla^{\top}\boldsymbol{w}\right)\boldsymbol{u}-\mu\left(\nabla^{\top}\boldsymbol{u}\right)\boldsymbol{w}\right)\cdot\boldsymbol{n}\,\mathrm{d}S. \tag{57}$$

According to the fundamental lemma of variational calculus, the integrant of the boundary integral needs two vanish independently from the volumetric term, which is the case if the computational domain Ω or the boundary conditions on $\partial\Omega$ are chosen appropriately. The first term of the boundary integral vanishes if $\partial\Omega\cap\partial\Omega_{\mathrm{f}}=\emptyset$ and therefore, $\nabla I=\mathbf{0}$ holds. It also vanishes if Dirichlet boundary conditions are prescribed at $\partial\Omega\cap\partial\Omega_{\mathrm{f}}$, leading to $\boldsymbol{w}=\mathbf{0}$ due to $\boldsymbol{w}\in H^{3}_{\mathrm{D}}$. The second term in the boundary integral vanishes if $I=0$ at the boundary. Alternatively, if no solid is present at the domain boundaries, i.e. $I=1$, the term $\left(\mu(\nabla^{\top}\boldsymbol{w})\boldsymbol{u}-\mu(\nabla^{\top}\boldsymbol{u})\boldsymbol{w}\right)\cdot\boldsymbol{n}=0$ is required, which is the same condition compared to the original weak form in equation (55), reflecting the fluid flow boundary conditions of the corresponding parts of $\partial\Omega_{\mathrm{f}}\subset\partial\Omega$.

Using this result of the viscous term, the whole domain formulation of the Navier–Stokes system (1) is given by

$$I\rho\dot{\boldsymbol{u}}=-I\nabla p+\nabla\cdot(I\mu\nabla\boldsymbol{u})+(\boldsymbol{u}-\boldsymbol{u}^{\mathrm{w}})\nabla\cdot(\mu\nabla I)+\rho I\boldsymbol{f}^{\mathrm{b}}, \tag{58a}$$

$$0=\nabla\cdot(I\boldsymbol{u})-\boldsymbol{u}^{\mathrm{w}}\cdot\nabla I. \tag{58b}$$

A.2.1. Different formulations for the left-hand side

Note that the left-hand side of equation (58*a*) can be reformulated according to

$$I\rho\dot{\boldsymbol{u}}=I\rho\frac{\partial\boldsymbol{u}}{\partial t}+I\rho(\nabla\boldsymbol{u})\boldsymbol{u}=\rho\left[\frac{\partial I\boldsymbol{u}}{\partial t}+\nabla(I\boldsymbol{u})\boldsymbol{u}\right]-\rho\boldsymbol{u}\left[\frac{\partial I}{\partial t}+\boldsymbol{u}\cdot\nabla I\right]=\rho(\boldsymbol{u}I)^{\cdot}-\rho\boldsymbol{u}\dot{I}. \tag{59}$$

In addition, the term can be given in conservation form as

$$I\left[\frac{\partial\rho\boldsymbol{u}}{\partial t}+\nabla\cdot(\rho\boldsymbol{u}\otimes\boldsymbol{u})\right]=\frac{\partial\rho I\boldsymbol{u}}{\partial t}+\nabla\cdot(\rho I\boldsymbol{u}\otimes\boldsymbol{u})-\rho\boldsymbol{u}\dot{I}. \tag{60}$$

The gradient and conservation form in equations (59) and (60) can be shown to be identical by using the mass balance:

$$\frac{\partial\rho I\boldsymbol{u}}{\partial t}+\nabla\cdot(\rho I\boldsymbol{u}\otimes\boldsymbol{u})=\frac{\partial I\boldsymbol{u}}{\partial t}+\rho\nabla(I\boldsymbol{u})\boldsymbol{u}+\boldsymbol{u}\left[I\frac{\partial\rho}{\partial t}+I\nabla\cdot(\rho\boldsymbol{u})\right]=\rho(\boldsymbol{u}I)^{\cdot} \tag{61}$$

since $I\partial_t\rho+I\nabla\cdot(\rho\boldsymbol{u})=0$. In absence of phase transformation processes, $\dot{I}=0$ holds, and equation (58*a*) can be written in the form

$$\frac{\partial\rho I\boldsymbol{u}}{\partial t}+\nabla\cdot(\rho I\boldsymbol{u}\otimes\boldsymbol{u})=-I\nabla p+\nabla\cdot(I\mu\nabla\boldsymbol{u})+(\boldsymbol{u}-\boldsymbol{u}^{\mathrm{w}})\nabla\cdot(\mu\nabla I)+\rho I\boldsymbol{f}^{\mathrm{b}}, \tag{62}$$

which is the formulation used in Aland *et al* [3]. In contrast, the gradient form $\rho(\boldsymbol{u}I)^{\cdot}$ is applied by Guo *et al* [25]. A special case of vanishing phase-transformation is an interface which exhibits no motion, i.e. $\partial_t I=0\ \wedge\ \boldsymbol{u}^{\mathrm{w}}\cdot\nabla I=0$. The last condition can be fulfilled by a zero wall velocity $\boldsymbol{u}=\mathbf{0}$ or a purely tangential velocity with $\boldsymbol{u}^{\mathrm{w}}\cdot\boldsymbol{n}=0$ as $\nabla I=-\delta_{\Gamma}\boldsymbol{n}$. A final special case is a boundary condition for uniform blowing or suction. Here, a non-vanishing normal wall velocity $\boldsymbol{u}^{\mathrm{w}}$ is considered, but the interface does not move at this velocity, as the wall velocity mimics fluid being blown out or sucked in through small holes that are modelled as being smeared over the complete wall, while the no-slip condition still applies.

A.2.2. Different formulations for the right-hand side

The right-hand side of equation (58*a*) may be adjusted by using the identity

$$\begin{aligned}\nabla\cdot(I\mu\nabla\boldsymbol{u})&=\nabla\cdot[\mu\nabla(I\boldsymbol{u})-\mu\boldsymbol{u}\otimes\nabla I]\\&=\nabla\cdot[\mu\nabla(I\boldsymbol{u})]-\boldsymbol{u}\nabla\cdot(\mu\nabla I)-\mu(\nabla\boldsymbol{u})\nabla I\end{aligned}$$

which yields

$$\frac{\partial(\rho I\boldsymbol{u})}{\partial t}+\nabla\cdot(\rho I\boldsymbol{u}\otimes\boldsymbol{u})=-I\nabla p+\nabla\cdot[\mu\nabla(I\boldsymbol{u})]-\mu(\nabla\boldsymbol{u})\nabla I-\boldsymbol{u}^{\mathrm{w}}\nabla\cdot(\mu\nabla I)+\rho I\boldsymbol{f}^{\mathrm{b}}. \tag{63}$$

For a vanishing wall velocity $\boldsymbol{u}^{\mathrm{w}} = \mathbf{0}$, this equation is identical to the one given by Beckermann *et al* [5, equation (13)], which is obtained by a volume averaging approach. Instead of evaluating $\mu(\nabla \boldsymbol{u})\nabla I$ directly, the authors in [5] approximate the term using a Darcy model, which is often used in connection with homogenised models for porous media flows. To this end,

$$\mu(\nabla \boldsymbol{u})\nabla I \approx h_{\mathrm{f}}\mu\,(\boldsymbol{u}-\boldsymbol{u}^{\mathrm{w}})\,\frac{1-\phi}{\delta_{\mathrm{d}}}\|\nabla\phi\| \tag{64}$$

is used, where ϕ is the phase-field variable which serves as the approximation of the indicator function $I \approx \phi$, while the surface Dirac distribution is approximated by $\delta_\Gamma \approx \|\nabla\phi\|$. The parameter h_{f} represents a dimensionless friction coefficient, which determines the additional dissipation added by the term within the diffuse interface. Following [5], the actual value of h_{f} is fitted in a linearised flow regime to match the conditions of linear velocity at the outskirts of the diffuse interface, which are

$$\boldsymbol{u}\,(\eta = -\delta_{\mathrm{d}}/2) = 0 \quad \text{and} \quad \boldsymbol{u}\,(\eta = \delta_{\mathrm{d}}/2) = \boldsymbol{u}_{\mathrm{ref}}\,(\eta = \delta_{\mathrm{d}}/2)\,. \tag{65}$$

Here, η denotes the surface normal coordinate, δ_{d} the diffuse interface width and $\boldsymbol{u}_{\mathrm{ref}}$ the reference solution of a Couette flow or the linearised regime of a Poiseuille flow. This ensures that in the bulk region $\Omega_{\phi=1}$, the velocity of the sharp interface theory is restored for these flows. For more general flows, the value of h_{f} needs to be fitted to the corresponding conditions that require the sharp interface solution. However, the argument put forward by [5] is that the value varies only slightly (in the range of a few %) as long as small interface widths are considered, for which a linearised velocity curve is a good approximation. For the present interface definitions (cf section 2.3), the values of h_{f} are 19.721 and 33.126 for the obstacle and well potential, respectively. Furthermore, the norm of the phase-field gradient may be obtained by assuming a phase-field equilibrium profile instead of determining it directly. Thus,

$$\|\nabla\phi\| = \frac{\pi}{\delta_{\mathrm{d}}}\sqrt{\phi\,(1-\phi)} \quad \text{and} \quad \|\nabla\phi\| = \frac{12}{\delta_{\mathrm{d}}}\phi\,(1-\phi) \tag{66}$$

can be used for both the obstacle and the well potential.

A.3. Whole domain formulation of the Chorin projection method

A Chorin type [11] projection method is commonly used for a time increment of the incompressible Navier–Stokes system. Subsequently, the different whole domain formulations for the corresponding pressure Poisson equation are given. Dividing the whole domain momentum balance (62) by ρ and a proceeding time integration over the interval $[t_n, t_{n+1}]$ yields

$$(I\boldsymbol{u})^{n+1} - (I\boldsymbol{u})^{n} = -\int_{t_n}^{t_{n+1}} \rho^{-1} I\nabla p \,\mathrm{d}t + \int_{t_n}^{t_{n+1}} \Phi \,\mathrm{d}t, \tag{67a}$$

$$\Phi = -\nabla\cdot(I\boldsymbol{u}\otimes\boldsymbol{u}) + \rho^{-1}\nabla\cdot(I\mu\nabla\boldsymbol{u}) + \rho^{-1}\,(\boldsymbol{u}-\boldsymbol{u}^{\mathrm{w}})\,\nabla\cdot(\mu\nabla I) + I\boldsymbol{f}^{\mathrm{b}}, \tag{67b}$$

with the abbreviation $(\cdot)^n = (\cdot)(\boldsymbol{x}, t_n)$. By defining the preliminary velocity field

$$I^n\boldsymbol{u}^{\mathrm{pre}} := I^n\boldsymbol{u}^n + \int_{t_n}^{t_{n+1}} \Phi \,\mathrm{d}t, \tag{68}$$

this gives rise to the projection step

$$(I\boldsymbol{u})^{n+1} = I^n\boldsymbol{u}^{\mathrm{pre}} - \int_{t_n}^{t_{n+1}} \rho^{-1} I\nabla p \,\mathrm{d}t. \tag{69}$$

By taking the divergence of equation (69) and demanding the continuity equation (58*b*) at the new time step, i.e. $\nabla\cdot(I\boldsymbol{u})^{n+1} - (\boldsymbol{u}^{\mathrm{w}}\cdot\nabla I)^{n+1} = 0$, the pressure Poisson equation

$$\int_{t_n}^{t_{n+1}} \nabla\cdot\left(\rho^{-1} I\nabla p\right)\,\mathrm{d}t = \nabla\cdot(I^n\boldsymbol{u}^{\mathrm{pre}}) - (\boldsymbol{u}^{\mathrm{w}}\cdot\nabla I)^{n+1} \tag{70}$$

is obtained. Different types of approximations for the time integration can be made. The easiest is to use an explicit Euler method to determine $\boldsymbol{u}^{\mathrm{pre}}$ in equation (68) and an implicit Euler method for the pressure term in equation (69), which gives rise to

$$I^n\boldsymbol{u}^{\mathrm{pre}} = I^n\boldsymbol{u}^n + \Delta t\Phi^n \tag{71a}$$

$$I^{n+1}\boldsymbol{u}^{n+1} = I^{n}\boldsymbol{u}^{\mathrm{pre}} - \Delta t\,\rho^{-1} I^{n+1}\nabla p, \tag{71b}$$

$$\nabla\cdot\left(\rho^{-1}I^{n+1}\nabla p\right) = \frac{1}{\Delta t}\left(\nabla\cdot\left(I^{n}\boldsymbol{u}^{\mathrm{pre}}\right) - \left(\boldsymbol{u}^{\mathrm{w}}\cdot\nabla I\right)^{n+1}\right), \tag{71c}$$

where Φ is determined according to equation (67*b*) and $\Delta t := t_{n+1} - t_n$ is the time step width.

A.4. Self-similar boundary layer solution

Subsequently, the theory used for the reference solution of the boundary layer flow benchmark is briefly introduced. A self-similar solution for wedge flows with a wedge angle of $\beta\pi/2$ is given by the Falkner–Skan equation [21]

$$f''' + ff'' + \beta\left(1 - f'^{2}\right) = 0, \tag{72}$$

which is a non-linear ordinary third-order differential equation. Thereby, $f(\tilde{\eta})$ is a dimensionless stream function, $(\cdot)' := \mathrm{d}(\cdot)/\mathrm{d}\tilde{\eta}$, the derivative with respect to the dimensionless coordinate

$$\tilde{\eta} = \frac{y}{L}\frac{\sqrt{Re}}{\delta^{*}}, \tag{73}$$

with

$$\delta^{*} = \sqrt{\frac{2}{m+1}\xi^{1-m}}, \quad m = \frac{\beta}{2-\beta}, \quad \xi = x/L. \tag{74}$$

The outer flow velocity obeys the power law $U(x) = U_{\mathrm{ref}}\xi^{m}$ with the reference velocity $U_{\mathrm{ref}} = U(\xi = 1)$. The overall velocity field $\boldsymbol{u} = u\boldsymbol{e}_x + v\boldsymbol{e}_y$ is given via

$$u = Uf', \quad v = -\sqrt{\frac{m+1}{2}\frac{\mu}{\rho}\frac{UL}{\xi}}\left(f + \frac{m-1}{m+1}\tilde{\eta}f'\right). \tag{75}$$

The boundary conditions for the Falkner–Skan equation (72) are

$$\lim_{\tilde{\eta}\to\infty} f' = 1, \quad f'(0) = 0, \quad f(0) = -v_{\mathrm{w}}\sqrt{\frac{2}{m+1}\frac{\rho}{\mu}\frac{\xi}{UL}}, \tag{76}$$

with a wall velocity v_{w} that can mimic uniform blowing or suction at the wall. As supplementary material, a matlab/GNU octave script is provided that solves the boundary value problem consisting of equations (75) and (76) for a number of x-locations with $\xi \in [0, 1]$. A shooting method employing a fourth-order Runge-Kutta integration method is used to solve up to $\tilde{\eta} = 5$, where the far-field boundary condition is applied. This solution can be used to determine the velocity field according to equation (75), which is used in this work both for the reference solution and to apply boundary conditions at the top. For the special case of $\beta = m = 0$, the Falkner–Skan equation simplifies to the Blasius equation for a flat plate with a constant outer velocity $U = U_{\mathrm{ref}} = \mathrm{const}$. The displacement velocity V can be determined by equation (75) for $\tilde{\eta} \to \infty$. In the special case without suction/blowing, i.e. $v_{\mathrm{w}} = 0$, $f(0) = 0$, the displacement velocity is independent of the x-coordinate, and

$$\lim_{\eta\to\infty} f - \tilde{\eta}f' = -1.2165 \tag{77}$$

holds, leading to equation (44) for the displacement velocity employed in this work. For $v_{\mathrm{w}} \neq 0$, the boundary conditions (76) depend on the x-coordinate, and thus, equation (75) must be solved with the corresponding boundary condition for each x-position to obtain the displacement velocity V. This is done by the provided script of the supplementary material.

For uniform suction, the similarity solution is characterised by a shape ratio of $H_{12} := \delta_1/\delta_2$, which decreases asymptotically from $H_{12}(x = 0) = 2.59$ to $\lim_{x\to\infty} H_{12} = 2$. Therefore a stationary boundary layer thickness is established at

$$-\frac{v_{\mathrm{w}}}{U}\sqrt{\frac{\rho U\hat{x}}{\mu}} = 2, \quad \frac{\hat{x}}{L} = \frac{4}{Re}\frac{U^{2}}{v_{\mathrm{w}}^{2}}, \tag{78}$$

and thus, for $H_{12} \leqslant 2.02$ cf [54, chapter 11.2.5]. This behaviour is reproduced by the solver script of the supplementary material.

References

[1] Abels H, Garcke H and Grün G 2012 Thermodynamically consistent, frame indifferent diffuse interface models for incompressible two-phase flows with different densities *Math. Mod. Methods Appl. Sci.* **22** 1150013
[2] Aguilar-Madera C, Flores-Cano J, Matías-Pérez V, Briones-Carrillo J and Velasco-Tapia F 2020 Computing the permeability and Forchheimer tensor of porous rocks via closure problems and digital images *Adv. Water Resour.* **142** 103616
[3] Aland S, Lowengrub J and Voigt A 2010 Two-phase flow in complex geometries: a diffuse domain approach *Comput. Mod. Eng. Sci.* **57** 77
[4] Anderson D M, McFadden G B and Wheeler A A 1998 Diffuse-interface methods in fluid mechanics *Ann. Rev. Fluid Mech.* **30** 139–65
[5] Beckermann C, Diepers H-J, Steinbach I, Karma A and Tong X 1999 Modeling melt convection in phase-field simulations of solidification *J. Comput. Phys.* **154** 468–96
[6] Bhopalam S R, Bueno J and Gomez H 2022 Elasto-capillary fluid–structure interaction with compound droplets *Comput. Methods Appl. Mech. Eng.* **400** 115507
[7] Blasius H 1908 Grenzschichten in flüssigkeiten mit kleiner reibung *Z. Math. Phys., Bd* **56** 1–37
[8] Brassel M and Bretin E 2011 A modified phase field approximation for mean curvature flow with conservation of the volume *Math. Methods Appl. Sci.* **34** 1157–80
[9] Bussoletti M, Gallo M, Bottacchiari M, Abbondanza D and Casciola C M 2024 Mesoscopic elasticity controls dynamin-driven fission of lipid tubules *Sci. Rep.* **14** 14003
[10] Chen L-Q 2008 Phase-field method of phase transitions/domain structures in ferroelectric thin films: a review *J. Am. Ceram. Soc.* **91** 1835–44
[11] Chorin A J 1968 Numerical solution of the Navier-Stokes equations *Math. Comput.* **22** 745–62
[12] Colagrossi A, Nikolov G, Durante D, Marrone S and Souto-Iglesias A 2019 Viscous flow past a cylinder close to a free surface: benchmarks with steady, periodic and metastable responses, solved by meshfree and mesh-based schemes *Comput. Fluids* **181** 345–63
[13] Coriell S, Boettinger W, Cordes M and Sekerka R 1981 Effect of gravity on coupled convective and interfacial instabilities during directional solidification *Adv. Space Res.* **1** 5–11
[14] Cusato N, Nabavizadeh S A and Eshraghi M 2023 A review of large-scale simulations of microstructural evolution during alloy solidification *Metals* **13** 1169
[15] Daubner S, Hoffrogge P W, Minar M and Nestler B 2023 Triple junction benchmark for multiphase-field and multi-order parameter models *Comput. Mater. Sci.* **219** 111995
[16] Daubner S, Weichel M, Reder M, Schneider D, Huang Q, Cohen A E, Bazant M Z and Nestler B 2025 Simulation of intercalation and phase transitions in nano-porous, polycrystalline agglomerates *npj Comput. Mater.* **11** 211
[17] Davis S H 1990 Hydrodynamic interactions in directional solidification *J. Fluid Mech.* **212** 241–62
[18] Eiken J 2012 Numerical solution of the phase-field equation with minimized discretization error *IOP Conf. Ser.: Mater. Sci. Eng.* **33** 012105
[19] Elmoghazy A, Heuer A, Kneer A, Reder M, Prahs A, Schneider D, Liebig W V and Nestler B 2024 Phase-field modeling of the morphological and thermal evolution of additively manufactured polylactic acid layers and their influence on the effective elastic mechanical properties *Prog. Addit. Manuf.* **10** 1–23
[20] Emmerich H 2008 Advances of and by phase-field modelling in condensed-matter physics *Adv. Phys.* **57** 1–87
[21] Falkner V and Skan S 1931 Lxxxv. solutions of the boundary-layer equations *London, Edinb. Dubl. Phil. Mag. J. Sci.* **12** 865–96
[22] Fan L, Reder M, Schneider D, Hinterstein M and Nestler B 2023 A phase-field model for ferroelectric materials–based on the multiphase-field method *Comput. Mater. Sci.* **230** 112510
[23] Gautier R, Biau D and Lamballais E 2013 A reference solution of the flow over a circular cylinder at re = 40 *Comput. Fluids* **75** 103–11
[24] Gomez H and Van der Zee K G 2017 Computational phase-field modeling *Encyclopedia of Computational Mechanics Second Edition* (Wiley) pp 1–35
[25] Guo Z, Yu F, Lin P, Wise S and Lowengrub J 2021 A diffuse domain method for two-phase flows with large density ratio in complex geometries *J. Fluid Mech.* **907** A38
[26] Hoffrogge P, Mukherjee A, Nani E, Amos P K, Wang F, Schneider D and Nestler B 2021 Multiphase-field model for surface diffusion and attachment kinetics in the grand-potential framework *Phys. Rev. E* **103** 033307
[27] Hoffrogge P W, Schneider D, Wankmüller F, Meffert M, Gerthsen D, Weber A, Nestler B and Wieler M 2023 Performance estimation by multiphase-field simulations and transmission-line modeling of nickel coarsening in FIB-SEM reconstructed Ni-YSZ SOFC anodes i: Influence of wetting angle *J. Power Sources* **570** 233031
[28] Hötzer J, Reiter A, Hierl H, Steinmetz P, Selzer M and Nestler B 2018 The parallel multi-physics phase-field framework pace3d *J. Comput. Sci.* **26** 1–12
[29] Hysing S, Turek S, Kuzmin D, Parolini N, Burman E, Ganesan S and Tobiska L 2009 Quantitative benchmark computations of two-dimensional bubble dynamics *Int. J. Numer. Methods Fluids* **60** 1259–88
[30] Iglisch R 1944 *Exakte Berechnung der Laminaren Grenzschicht an der läNgsangeströMten Ebenem Platte mit Homogener Absaugung* vol 8b (Schriften der Deutschen Akademie der Luftfahrtforschung, 26th Ian)
[31] Jacqmin D 1999 Calculation of two-phase Navier–Stokes flows using phase-field modeling *J. Comput. Phys.* **155** 96–127
[32] Kannenberg T, Prahs A, Svendsen B, Nestler B and Schneider D 2024 Chemo-mechanical benchmark for phase-field approaches *Modelling Simul. Mater. Sci. Eng.* **33** 015004
[33] Kim J 2012 Phase-field models for multi-component fluid flows *Commun. Comput. Phys.* **12** 613–61
[34] Kim J, Lee S and Choi Y 2014 A conservative Allen–Cahn equation with a space–time dependent Lagrange multiplier *Int. J. Eng. Sci.* **84** 11–17
[35] Li L, Stoellinger M and Mousaviraad M 2024 Rigorous benchmarking of an iterative IBM solver by comparison to body-fitted mesh results *Comput. Fluids* **277** 106281
[36] Li Q, Liang L, Gerdes K and Chen L-Q 2012 Phase-field modeling of three-phase electrode microstructures in solid oxide fuel cells *Appl. Phys. Lett.* **101** 033909
[37] Li X, Lowengrub J, Rätz A and Voigt A 2009 Solving PDEs in complex geometries: a diffuse domain approach *Commun. Math. Sci.* **7** 81–107

[38] Liu C-S and Chang J-R 2008 The lie-group shooting method for multiple-solutions of Falkner–Skan equation under suction–injection conditions *Int. J. Non-Linear Mech.* **43** 844–51
[39] Lorez F and Pundir M 2025 Exploring dynamic contact of soft solids with an Eulerian phase-field approach *Int. J. Solids Struct.* **323** 113621
[40] Lowengrub J and Truskinovsky L 1998 Quasi–incompressible Cahn–Hilliard fluids and topological transitions *Proc. R. Soc. A* **454** 2617–54
[41] Lu L-X, Sridhar N and Zhang Y-W 2018 Phase field simulation of powder bed-based additive manufacturing *Acta Mater.* **144** 801–9
[42] Mamivand M, Zaeem M A and Kadiri H E 2013 A review on phase field modeling of martensitic phase transformation *Comput. Mater. Sci.* **77** 304–11
[43] Miyoshi E, Takaki T, Ohno M, Shibuta Y, Sakane S, Shimokawabe T and Aoki T 2017 Ultra-large-scale phase-field simulation study of ideal grain growth *npj Comput. Mater.* **3** 25
[44] Mokbel D, Abels H and Aland S 2018 A phase-field model for fluid–structure interaction *J. Comput. Phys.* **372** 823–40
[45] Nestler B, Garcke H and Stinner B 2005 Multicomponent alloy solidification: phase-field modeling and simulations *Phys. Rev. E* **71** 041609
[46] Nestler B, Wendler F, Selzer M, Stinner B and Garcke H 2008 Phase-field model for multiphase systems with preserved volume fractions *Phys. Rev. E* **78** 011604
[47] Oktasendra F, Rennick M, Avis S J, Panter J R and Kusumaatmaja H 2025 The diffuse solid method for wetting and multiphase fluid simulations in complex geometries *Phys. Fluids* **37** 052103
[48] Punke M, Salvalaglio M, Voigt A and Wise S M 2025 A non-isothermal phase-field crystal model with lattice expansion: analysis and benchmarks *Modelling Simul. Mater. Sci. Eng.* **33** 025007
[49] Reder M, Hoffrogge P W, Schneider D and Nestler B 2022 A phase-field based model for coupling two-phase flow with the motion of immersed rigid bodies *Int. J. Numer. Methods Eng.* **123** 3757–80
[50] Reder M, Prahs A, Schneider D and Nestler B 2024 Viscous stress approximations in diffuse interface methods for two-phase flow based on mechanical jump conditions *Comput. Methods Appl. Mech. Eng.* **432** 117341
[51] Reder M, Schneider D, Wang F, Daubner S and Nestler B 2021 Phase-field formulation of a fictitious domain method for particulate flows interacting with complex and evolving geometries *Int. J. Numer. Methods Fluids* **93** 2486–507
[52] Reiter A 2021 Some Implications of Constraints in Phasefield Models *PhD Thesis* Karlsruher Institut für Technologie (KIT) 38.04.04; LK 01
[53] Rubinstein J and Sternberg P 1992 Nonlocal reaction–diffusion equations and nucleation *IMA J. Appl. Math.* **48** 249–64
[54] Schlichting H and Gersten K 2016 *Boundary-Layer Theory* (Springer)
[55] Schoof E, Schneider D, Streichhan N, Mittnacht T, Selzer M and Nestler B 2018 Multiphase-field modeling of martensitic phase transformation in a dual-phase microstructure *Int. J. Solids Struct.* **134** 181–94
[56] Steinbach I, Pezzolla F, Nestler B, Seeßelberg M, Prieler R, Schmitz G J and Rezende J L 1996 A phase field concept for multiphase systems *Physica D* **94** 135–47
[57] Steinbach I and Salama H 2023 *Lectures on Phase Field* 1st edn (Springer)
[58] Sun Y and Beckermann C 2007 Sharp interface tracking using the phase-field equation *J. Comput. Phys.* **220** 626–53
[59] Tourret D, Liu H and LLorca J 2022 Phase-field modeling of microstructure evolution: recent applications, perspectives and challenges *Prog. Mater. Sci.* **123** 100810
[60] Weichel M, Reder M, Daubner S, Klemens J, Burger D, Scharfer P, Schabel W, Nestler B and Schneider D 2025 Modeling the drying process in hard carbon electrodes based on the phase-field method *Phys. Rev. Mater.* **9** 035403
[61] Yu F, Guo Z and Lowengrub J 2020 Higher-order accurate diffuse-domain methods for partial differential equations with Dirichlet boundary conditions in complex, evolving geometries *J. Comput. Phys.* **406** 109174
[62] Yu H-C, Chen H-Y and Thornton K 2012 Extended smoothed boundary method for solving partial differential equations with general boundary conditions on complex boundaries *Modelling Simul. Mater. Sci. Eng.* **20** 075008
[63] Zheng X, Yazdani A, Li H, Humphrey J D and Karniadakis G E 2020 A three-dimensional phase-field model for multiscale modeling of thrombus biomechanics in blood vessels *PLoS Comput. Biol.* **16** e1007709